MicroRNA-19a-PTEN Axis Is Involved in the Developmental Decline of Axon Regenerative Capacity in Retinal Ganglion Cells

Heather K. Mak,[1] Jasmine S.Y. Yung,[1] Robert N. Weinreb,[2,3] Shuk Han Ng,[1] Xu Cao,[1] Tracy Y.C. Ho,[1] Tsz Kin Ng,[1] Wai Kit Chu,[1] Wing Ho Yung,[4,5] Kwong Wai Choy,[6] Chi Chiu Wang,[6] Tin Lap Lee,[4] and Christopher Kai-shun Leung[1]

[1]Department of Ophthalmology and Visual Sciences, The Chinese University of Hong Kong, Hong Kong, PRC; [2]Hamilton Glaucoma Center, Shiley Eye Institute, University of California, San Diego, La Jolla, CA, USA; [3]Department of Ophthalmology, University of California, San Diego, La Jolla, CA, USA; [4]School of Biomedical Sciences, Faculty of Medicine, The Chinese University of Hong Kong, Hong Kong, PRC; [5]Gerald Choa Neuroscience Centre, The Chinese University of Hong Kong, Hong Kong, PRC; [6]Department of Obstetrics and Gynecology, Prince of Wales Hospital, The Chinese University of Hong Kong, Hong Kong, PRC

Irreversible blindness from glaucoma and optic neuropathies is attributed to retinal ganglion cells (RGCs) losing the ability to regenerate axons. While several transcription factors and proteins have demonstrated enhancement of axon regeneration after optic nerve injury, mechanisms contributing to the age-related decline in axon regenerative capacity remain elusive. In this study, we show that microRNAs are differentially expressed during RGC development and identify microRNA-19a (miR-19a) as a heterochronic marker; developmental decline of miR-19a relieves suppression of phosphatase and tensin homolog (PTEN), a key regulator of axon regeneration, and serves as a temporal indicator of decreasing axon regenerative capacity. Intravitreal injection of miR-19a promotes axon regeneration after optic nerve crush in adult mice, and it increases axon extension in RGCs isolated from aged human donors. This study uncovers a previously unrecognized involvement of the miR-19a-PTEN axis in RGC axon regeneration, and it demonstrates therapeutic potential of microRNA-mediated restoration of axon regenerative capacity in optic neuropathies.

INTRODUCTION

Developmental decline in axon regenerative capacity is well recognized in retinal ganglion cells (RGCs),[1,2] which leads to permanent loss in visual function in all forms of optic neuropathies, including glaucoma, a leading cause of irreversible blindness. Failure to regenerate axons in RGCs has been attributed to external growth-inhibiting factors in the central nervous system (CNS)[3–8] and intrinsic molecular mechanisms that regulate cell growth.[9–13] Although a growing number of transcription factors and proteins have been demonstrated to enhance axon regenerative potential in injured RGCs,[14–20] the signaling pathways that govern axon extension during development remain poorly understood.

MicroRNAs (miRNAs) are short non-coding RNA molecules that function primarily as posttranscriptional regulators.[21,22] Although many studies have demonstrated the involvement of miRNAs in the development and differentiation of cortical neurons in mice and *C. elegans*,[23–33] it is largely unclear whether miRNAs are involved in the regulation of developmental decline in axon regenerative capacity of mammalian RGCs. We set out to identify miRNAs that are differentially expressed in the RGCs during development and investigate whether manipulating their levels can restore a molecular environment conducive for axon regeneration in aged or injured RGCs. Using microarray analysis, we show that the levels of microRNA-19a (miR-19a) are substantively downregulated in the RGCs during development and that its downregulation is inversely associated with the expression of phosphatase and tensin homolog (PTEN), a key suppressor of optic nerve regeneration.[14] PTEN is a predicted target of miR-19a;[34] miR-19a has been implicated in the regulation of PTEN expression in a variety of pathological and physiological conditions, such as the PTEN hamartoma tumor syndromes,[35] regulation of glycogen synthesis in hepatocytes,[36] and regulation of axon outgrowth in embryonic cortical neurons.[32] However, our understanding of the involvement of the miR-19a-PTEN axis in the developmental decline of axon regenerative capacity remains incomplete. Specifically, it is unclear whether miR-19a can resuscitate the loss of axon regenerative capacity in adult RGCs. In this study, we demonstrate the inverse relationship between miR-19a and PTEN to be developmentally regulated, which coincides with the age-related decline of axon regenerative capacity in RGCs; increasing the levels of miR-19a in RGCs suppresses PTEN expression and significantly improves axon regeneration *in vivo* after optic nerve crush in mice, as well as in RGCs isolated from aged human donors. Our results reveal a previously unrecognized involvement of the miR-19a-PTEN axis as a heterochronic marker for the developmental regulation of axon regenerative capacity.
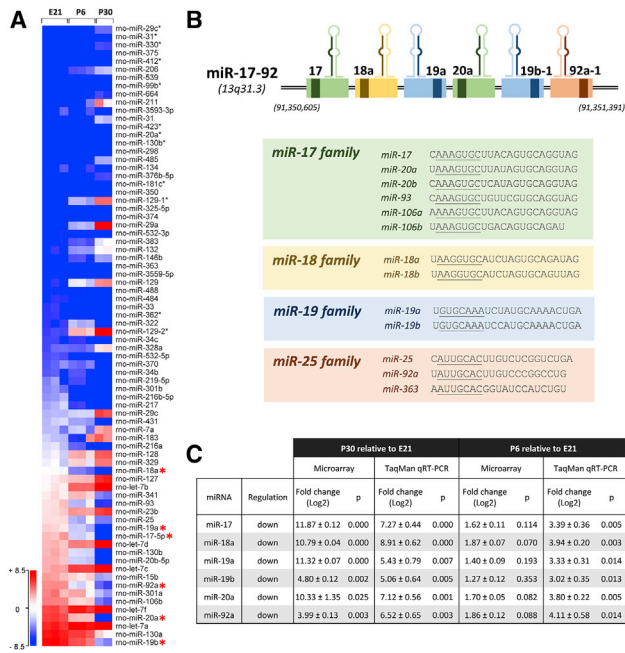
Figure 1. miRNAs Are Differentially Expressed in RGCs during Development

(A) A representative heatmap of miRNA expression profiles constructed from a microarray analysis of retinal ganglion cells (RGCs) purified from embryonic day 21 (E21, n = 3 biological replicates), postnatal day 6 (P6, n = 3 biological replicates), and P30 (n = 2 biological replicates) Sprague-Dawley (SD) rats, showing 76 endogenously expressed miRNAs with significant differential expression (≥ 4-fold changes in expression levels) during development. Developmental ages (as biological replicates) are indicated in columns, and differentially expressed miRNAs are indicated in rows. All six members of the miR-17-92 cluster (red asterisks) were found to have significant downregulation from E21 to P30 (right panel). Blue (−8.5) and red (+8.5) in the color-coding scale represent relative low and high normalized miRNA expressions, respectively. A two-tailed moderated t test with a Benjamini-Hochberg correction for false discovery rate was used to compare the means of miRNA microarray expression values between E21 and P6 and between E21 and P30. A list of the 76 miRNAs can be found in Table S1, and all other microarray data that support the findings of this study have been deposited in the National Center for Biotechnology Information Gene Expression Omnibus (GEO: GSE102458). (B) Illustration of the polycistronic miR-17-92 cluster region on human chromosome 13 (chromosome 15 for rats). Precursor transcripts derived from the miR-17-92 gene cluster contains six tandem stem-loop hairpin structures that yield six mature miRNAs: miR-17, miR-18a, miR-19a, miR-20a, miR-19b, and miR-92a. The miRNAs can be categorized into four miRNA families according to their conserved seed sequences (underlined). (C) Downregulation of the six miRNAs from E21 to P30 and from E21 to P6 was confirmed by TaqMan qRT-PCR (E21 vs. P6, miR-17-5p, p = 0.005; miR-18a, p = 0.003; miR-19a, p = 0.014; miR-19b, p = 0.013; miR-20a, p = 0.005; miR-92a, p = 0.014; E21 vs. P30, miR-17-5p, p = 0.0004; miR-18a, p = 0.001; miR-19a, p = 0.007; miR-19b, p = 0.005; miR-20a, p = 0.001; miR-92a, p = 0.003; n = 3 biological replicates for each age group). An unpaired two-tailed Student's t test was used for TaqMan comparisons. All values are shown as mean ± SEM.

RESULTS

Developmental Decline in Axon Regenerative Capacity Coincides with a Decreased Expression of miR-17-92 in RGCs

To examine developmental decline of axon regenerative capacity in RGCs, we isolated RGCs from Sprague-Dawley (SD) rats using CD90.1 magnetic microbeads (Miltenyi Biotec) (Figure S1A) and

showed that neurites extended from postnatal day 6 (P6) and P30 RGCs were 74.4% ± 2.7% (mean ± SEM) and 88.4% ± 0.7% shorter, respectively, than those from embryonic day 21 (E21) RGCs (p < 0.001) on day 14 in vitro (Figure S1B). We hypothesized that miRNAs, as key regulators of post-transcriptional gene expression during development, axon extension, and degeneration in cortical neurons,[31,33,37–42] would contribute to the developmental decline of axon regenerative capacity in RGCs. Using microarrays (Agilent Technologies) to screen for differential expression of miRNAs in the RGCs during development, we found that 76 miRNAs had more than a 4-fold difference in the expression levels between E21 and P30 RGCs, among which 32 (42%) were upregulated and 44 (58%) were downregulated (Figure 1A). The top three miRNAs with the greatest fold change (i.e., miR-17, miR-20b, and miR-19a) were downregulated from E21 to P30 RGCs (Table S1). Two of these miRNAs (miR-17 and miR-19a) belong to a highly conserved single polycistronic cluster, the miR-17-92 cluster (Figure 1B).[43] The other members of the miR-17-92 cluster (miR-18a, miR-19b, miR-20a, and miR-92a) were also downregulated from E21 to P30 (p ≤ 0.025) (Figure 1C). TaqMan qRT-PCR confirmed that the expression levels of miR-17, miR-18a, miR-19a, miR-19b, miR-20a, and miR-92a in the RGCs decreased substantively from E21 to P30 (p ≤ 0.007) and from E21 to P6 (p ≤ 0.014) (Figure 1C). Taken together, the developmental decline of axon regenerative capacity in the RGCs parallels the substantial decreases in the expression levels of the miR-17-92 family members.

We searched potential downstream targets of the miR-17-92 family members using TargetScan that may connect to axon projection or regeneration and clustered a total of 6,759 predicted targets according to their associated biological processes using the PANTHER classification system (version 11).[44] There were 314 downstream targets with a significant association (2.12-fold enrichment) with "neuron projection development" (Table S2). Within the 314 targets, 7 were found to be significantly related to "regulation of axon regeneration" (17.13-fold enrichment), that is, EPHA4, IGF1R, MAP2K1, NDEL1, PTEN, RGMA, and SCARF1.[14,45–50] The TargetScan context++ score percentile rank[51,52] was then referenced to evaluate the preferential binding of each of the miR-17-92 miRNA members to the relative efficacy of mRNA repression, in which PTEN showed the highest score (76%) compared with the other targets (range, 15%–32%). PTEN is a negative regulator of mTOR (mechanistic target of rapamycin), a key regulator of cell growth.[53–58] Unlike other miR-17-92 family members having only one binding site on the PTEN 3′ UTR, miR-19a and miR-19b have three binding sites on the PTEN 3′ UTR in humans and two in mice. As genetic deletion of Pten and Socs3, a suppressor of cytokine signaling inhibiting STAT3 activation, has been shown to synergistically promote axon regeneration after optic nerve crush,[17] we also searched for potential binding of the miR-17-92 family members on the SOCS3 3′ UTR and found that only miR-19a and miR-19b contain predicted binding sites on the 3′ UTR sequences of PTEN and SOCS3. miR-19a and miR-19b differ from each other only by 1 nucleotide, and the predicted locations of complementary binding onto the PTEN and SOCS3 3′ UTRs are the same in rodents and humans. With the expression level of miR-19a in
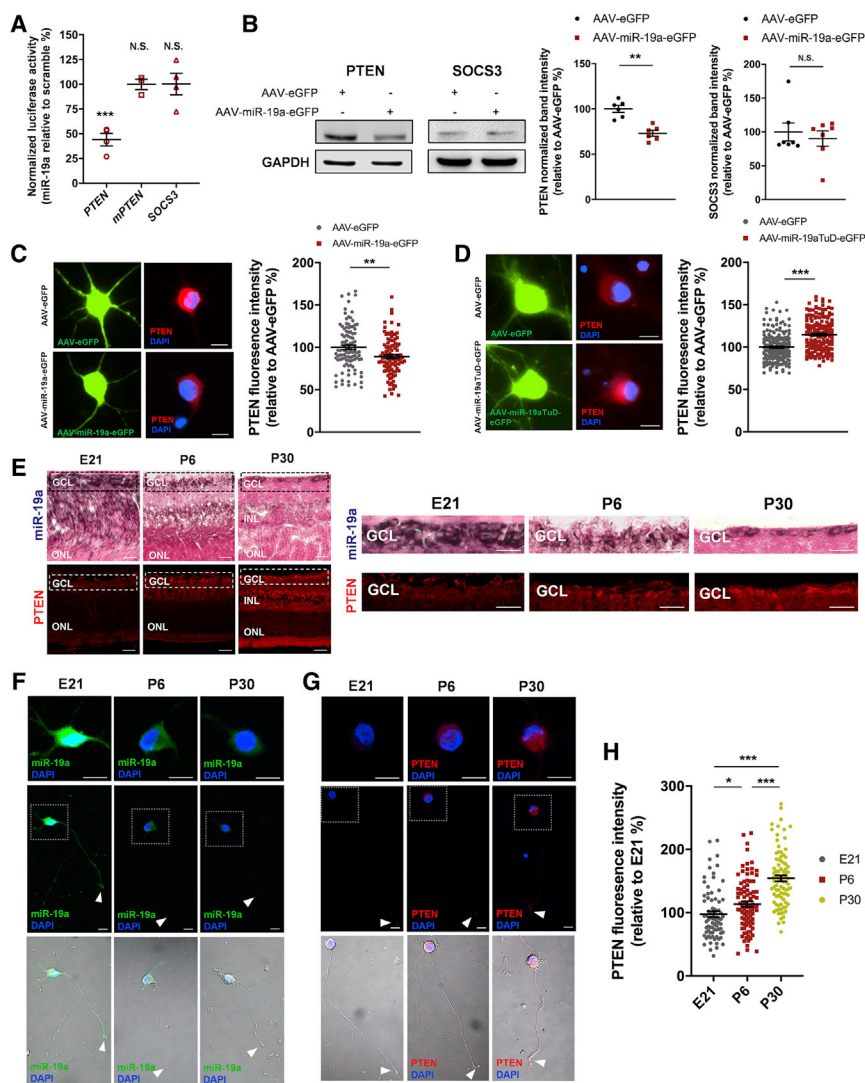
Figure 2. Developmental Decline of miR-19a Is Associated with Increased PTEN Expression in RGCs

(A) Dual luciferase assays of *PTEN*, *mPTEN*, and *SOCS3* 3′ UTR after transfection with miR-19a mimic or scramble oligonucleotides in P6 RGCs. Only *PTEN* 3′ UTR, but not *mPTEN* or *SOCS3* 3′ UTR, was significantly suppressed by miR-19a (*PTEN*, p = 0.0001; *mPTEN*, p = 0.987; *SOCS3*, p = 0.976; n = 3–4 experimental replicates). Firefly luciferase was normalized to *Renilla* activity. See also Figure S2. (B) Western blots of PTEN and SOCS3 in P6 RGCs after transduction with AAV-miR-19a-EGFP or AAV-EGFP (left). miR-19a significantly reduced PTEN (*PTEN*, p = 0.001; n = 6 experimental replicates), but not SOCS3 (*SOCS3*, p = 0.869; n = 7 experimental replicates) (right). Values were normalized to GAPDH or β-actin. (C and D) Immunofluorescence images of PTEN (red) in P6 RGCs with AAV-miR-19a-EGFP (green) (C) or AAV-miR-19aTuD-EGFP (green) (D). Scale bars, 10 μm. Single-cell PTEN intensity was significantly lower in AAV-miR-19a-EGFP-transduced RGCs (p = 0.002; n = 100 RGCs) and higher in AAV-miR-19aTuD-EGFP-transduced RGCs (p < 0.0001; n = 183 RGCs), compared with control (n = 327 RGCs). See also Figure S3. (E) In situ hybridization (ISH) and immunohistofluorescence images of endogenous miR-19a (upper panel) and PTEN (lower panel), respectively, in E21, P6, and P30 retinas. Boxed areas are magnified on the right. Scale bars, 25 μm. GCL, ganglion cell layer; INL, inner nuclear layer; ONL, outer nuclear layer. (F) ISH images of endogenous miR-19a (green) in E21, P6, and P30 RGCs. Boxed areas are magnified above. Scale bars, 10 μm. Axon growth cones are indicated by arrowheads. (G) Immunofluorescence images of endogenous PTEN (red) in E21, P6, and P30 RGCs. Boxed areas are magnified above. Scale bars, 10 μm. Axon growth cones are indicated by arrowheads. (H) Single-cell PTEN intensity significantly increased from E21 (n = 78 RGCs) to P6 (E21 vs. P6, p = 0.047; n = 89 RGCs) and to P30 (E21 vs. P30, p < 0.0001; P6 vs. P30, p < 0.0001; n = 88 RGCs). All values are shown as mean ± SEM. Unpaired two-tailed Student's t test was used for all comparisons: *p < 0.05, **p < 0.01, ***p < 0.001. N.S., not significant.

RGCs showing a greater reduction during development compared with miR-19b (Figure 1C; Table S1), we hypothesized that miR-19a is an important upstream regulator controlling the expression of PTEN and SOCS3 during development that contributes to the decline in axon regenerative capacity in mature RGCs.

Endogenous Expression of miR-19a Is Inversely Associated with PTEN in RGCs

To validate direct binding of miR-19a onto the 3′ UTR binding sites of *PTEN* and *SOCS3* in the RGCs, we performed dual luciferase reporter assays in purified RGCs transfected with dual luciferase reporter plasmids containing *PTEN* or *SOCS3* 3′ UTR sequences and oligonucleotides of miR-19a mimics or scramble (control) sequences (Figures S2A and S2B). *PTEN* luciferase activity decreased by 55.9% ± 6.4% (p < 0.001) whereas *SOCS3* luciferase activity showed no significant

difference (p = 0.976) in RGCs transfected with miR-19a oligonucleotides versus those transfected with scramble oligonucleotides (Figure 2A). Suppression of *PTEN* by miR-19a was relieved when the miR-19a binding site was mutated (Figure 2A). Among the members of the miR-17-92 cluster, miR-19a attained the greatest *PTEN* suppression in the RGCs (Figure S2C). We then examined whether overexpression of miR-19a in RGCs via transduction with enhanced green fluorescent protein-tagged adeno-associated virus (AAV-EGFP) (Figure S3A) would decrease the protein expression levels of PTEN and SOCS3. Immunoblots of AAV-miR-19a-EGFP-transduced RGCs revealed a significant reduction in PTEN (25.9% ± 0.04%, p = 0.001), but not SOCS3 (p = 0.869), protein expression, compared with RGCs transduced with AAV-EGFP (Figure 2B). Single-cell immunocytofluorescence staining further supported that overexpression of miR-19a decreased the level of PTEN expression by 10.8% ± 2.3%

(p = 0.002) (Figure 2C), whereas inhibition of miR-19a in RGCs, via AAV transduction of a tough decoy (TuD) miRNA inhibitor[59] (AAV-miR-19TuD-EGFP) containing two miR-19a binding sites per transcribed RNA secondary structure (Figures S3A and S3B), resulted in a 14.7% ± 1.4% increase in PTEN expression (p < 0.001) (Figure 2D), compared with controls. The endogenous expression of miRNA-19a and PTEN exhibited a reciprocal relationship in the retina during development (Figure 2E). In agreement with the Taq-Man qRT-PCR assay of miR-19a levels in purified RGCs, in situ hybridization (ISH) showed that miR-19a expression, which was largely localized to the ganglion cell layer, decreased from E21 to P6 and to P30 retinas. PTEN expression detected by immunohistochemistry, in contrast, increased from E21 to P6 and to P30 retinas. ISH in purified RGCs revealed that miR-19a was strongly expressed in the cytoplasm, axons, and growth cones of E21 RGCs, but was only weakly expressed in the cytoplasm, and undetectable in the growth cones, in P6 and P30 RGCs (Figure 2F). PTEN, in contrast, was minimally expressed in E21 RGCs, weakly expressed in the cytoplasm of P6 RGCs, and moderately expressed in the cytoplasm, axons, and growth cones in P30 RGCs (Figure 2G). P30 RGCs showed 1.6-fold and 1.4-fold increases in endogenous PTEN expression compared with E21 and P6 RGCs, respectively (p < 0.001) (Figure 2H). Collectively, our data support that the developmental downregulation of miR-19a is connected to an upregulation of PTEN expression in RGCs.

miR-19a Augments Axon Regeneration in Mature Rodent RGCs

We reasoned that increasing the level of miR-19a in mature RGCs would partially restore their capacity to regenerate axons after optic nerve injury. To study axon regeneration, we measured (1) the length of axon extension of RGCs in a microfluidic chamber, (2) the rate of axon extension in isolated RGCs using time-lapse imaging, and (3) the number of regenerating RGC axons after optic nerve crush in C57BL/6J mice. The microfluidic chamber is composed of two compartments separated by microgrooves (Figure S4A). This creates a difference in hydrostatic pressure and permits only axons to extend into the opposing compartment, isolating axons from cell bodies. Immunofluorescence staining confirmed the segregation of TAU-positive axons from MAP2-positive somata and dendrites in their respective compartments (Figures S4B and S4C). At day 14 in vitro, axon lengths of P6 RGCs transduced with AAV-miR-19a-EGFP were 2.9 ± 0.5-fold longer compared with those transduced with AAV-EGFP (p = 0.034) (Figure 3A). Inhibiting miR-19a with AAV-miR-19a-TuD significantly decreased axon extension by 59.6% ± 1.4% compared with the control vector (p < 0.001) (Figures S4D and S4E). To study the rate of axon extension, P6 RGCs at day14 in vitro were trypsinized and replated onto glass-bottom dishes for time-lapse imaging of individual RGCs. RGCs transduced with AAV-miR-19a-EGFP extended axons at a faster rate (17.4 ± 2.1 μm/h) compared with those transduced with AAV-EGFP (7.0 ± 2.1 μm/h) (p < 0.001) (Figures 3B and 3C; Videos S1 and S2). The mean length of axon extension was also greater in AAV-miR-19a-EGFP-transduced RGCs (108.4 ± 18.1 μm) than in the AAV-EGFP-transduced RGCs (47.8 ± 11.5 μm) (p = 0.019). There were no significant differences

in soma diameter, soma circularity, and baseline axon lengths (p ≥ 0.273) between the two groups.

To investigate the effects of overexpression of miR-19a on RGC axon regeneration in vivo, AAV-miR-19a-EGFP (n = 8 mice) or AAV-EGFP (n = 8 mice) was injected into the vitreous of a randomly selected eye in 16 C57BL/6J mice (Figure 3D). Optic nerve crush was performed at 3–4 weeks after intravitreal injection (in vivo imaging using confocal scanning laser ophthalmoscopy showed that fluorescent intensity of AAV-transduced RGCs peaked at 2–3 weeks) (Figure S5A). Cholera toxin subunit B (CTB) was then injected into the vitreous 3–4 weeks after optic nerve crush, and the number of CTB-positive axons was measured at every 0.5 mm from the crush site. Immunofluorescence staining of GAP43 confirmed that CTB-positive axons were regenerating axons (Figure S5B). AAV-miR-19a-EGFP-injected eyes had a greater number of regenerating axons compared with AAV-EGFP-injected eyes (multivariable linear mixed modeling adjusting for multiple comparisons at different distances from the crush site, p = 0.004) (Figures 3E and 3F). Overexpression of miR-19a also improved RGC survival following optic nerve crush compared with controls (p = 0.006) (Figures S5C and S5D).

miRNA-19a Promotes Axon Regeneration in Human Adult RGCs

Similar to rodent RGCs, we observed a significantly higher level of miR-19a expression in human fetal RGCs compared with aged RGCs purified from human donor eyes (Figure 4A). We next examined whether overexpression of miR-19a was able to augment the axon regenerative potential of aged RGCs isolated from adult human donor retinas. RGC axon length and total neurite length (i.e., length of axons and dendrites) were measured and analyzed after 2 weeks of AAV-mediated transduction of miR-19a-EGFP or EGFP. The frequency distributions of axon length and total neurite length were right shifted for RGCs transduced with miR-19a-EGFP (n = 60 RGCs) compared with those transduced with the control vector (n = 61 RGCs) (n = 121 total RGCs isolated from two human donors aged 69 and 75 years) (Figure 4B). Axon length and total neurite length of the miR-19a-EGFP-transduced RGCs were 1.3-fold (p = 0.041) and 1.7-fold (p < 0.001) longer, respectively, compared with those of the controls.

DISCUSSION

While a number of transcription factors and proteins have been implicated in the regulation of axon regeneration, why mature RGCs lose their intrinsic ability to extend axons remains largely unexplained. By isolating RGCs from the retina at different ages during development, our study uncovers miR-19a to be a heterochronic marker that drastically decreases in expression during the maturation of RGCs, which relieves the suppression of PTEN and contributes to the developmental decline of axon regenerative capacity (Figure 4C).

miRNA-19a has been demonstrated to regulate neural progenitor cell migration during neuronal development in the hippocampus and enhance axon growth in embryonic cortical neurons.[32,42] Its role in
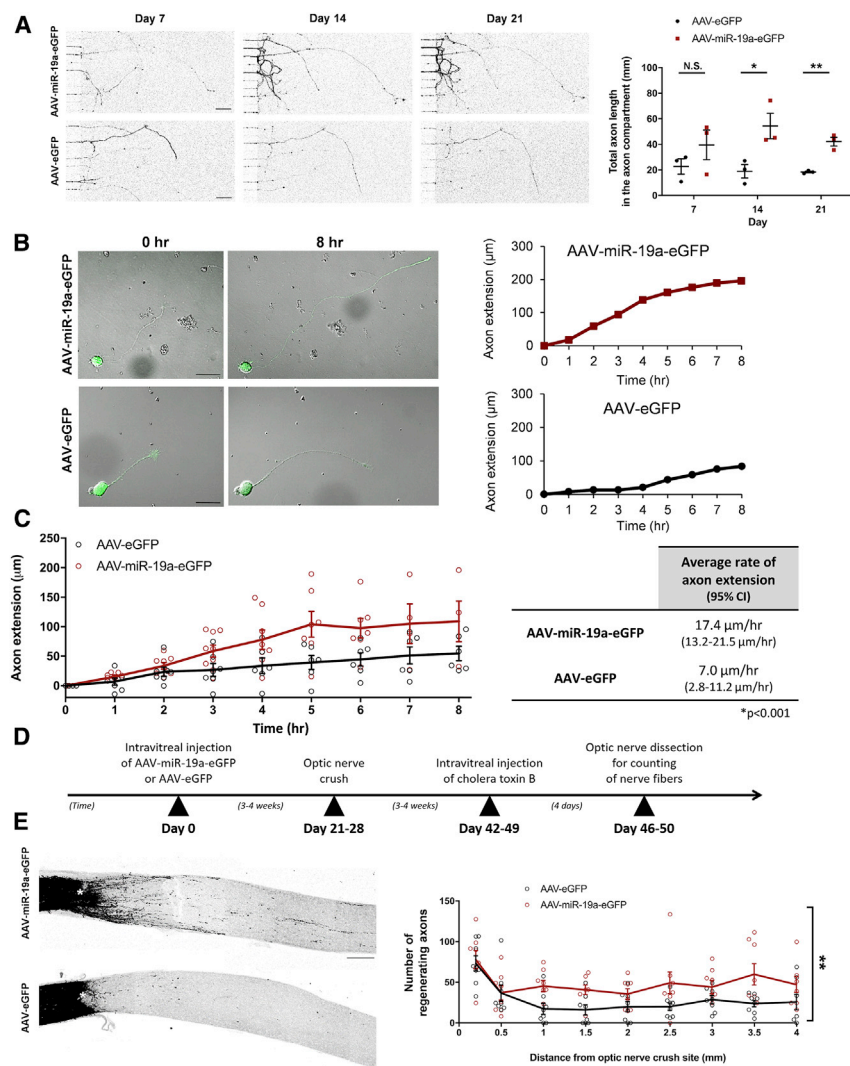
**Figure 3. miR-19a Augments Axon Regeneration in Mature Rodent RGCs**

(A) Serial fluorescence images of cropped image areas of the axonal compartment of microfluidic chambers with P6 RGCs transduced with AAV-miR-19a-EGFP or AAV-EGFP at 7, 14, and 21 days in vitro. Total axon lengths in the axonal compartment were significantly longer in RGCs transduced with AAV-miR-19a-EGFP (day 7, p = 0.264; day 14, p = 0.034; day 21, p = 0.002; n = 3 experimental replicates) than with AAV-EGFP (n = 3 experimental replicates). Scale bars, 100 μm. An unpaired two-tailed Student's t test was used for all comparisons. See also Figure S4. (B) Time-lapse microscopy images (left) showing axon extension of P6 RGCs transduced with AAV-miR-19a-EGFP (top) or AAV-EGFP (bottom). Scale bars, 25 μm. (C) The rate of axon extension of AAV-miR-19a-EGFP-transduced RGCs (n = 9 RGCs from 7 experimental replicates; 17.4 μm/h, 95% confidence interval [CI]: 13.2–21.5 μm/h) was significantly faster than that of AAV-EGFP-transduced RGCs (n = 7 RGCs from 5 experimental replicates; 7.0 μm/h, 95% CI: 2.8–11.2 μm/h). Multivariable linear mixed model was used for comparison after adjusting for comparisons at multiple time points after axotomy (p < 0.0001). (D) Timeline for evaluation of axon regeneration in C57BL/6 mice after optic nerve crush. (E) Fluorescence images of optic nerve sections from eyes intravitreally injected with AAV-miR-19a-EGFP (top) or AAV-EGFP (bottom). Regenerating axons were labeled with cholera toxin B (black). The crush site is indicated by an asterisk. Scale bars, 100 μm. (F) The numbers of regenerating axons were significantly greater in AAV-miR-19a-EGFP-transduced eyes (n = 8 mice) than in AAV-EGFP-transduced eyes (n = 8 mice). Multivariable linear mixed modeling was used for comparison after adjusting for comparisons at multiple distances from the crush site (p = 0.004). All values are shown as mean ± SEM. *p < 0.05, **p < 0.01, ***p < 0.001. N.S., not significant.

the retina, however, has not been previously investigated. Note that downregulation of miR-19a in the RGCs during development was not only observed in rodents, but also in RGCs isolated from fetal and aged humor donors (Figure 4A). Increasing the levels of miR-19a in the RGCs not only promoted axon regeneration in young adult rodents (optic nerve crush was performed at the age of ∼2 months), but it also enhanced axon regeneration in RGCs isolated from human donors at 69–75 years of age (Figure 4B). In other words, the involvement of the miR-19a-PTEN axis in the regulation of axon extension or regeneration is conserved in rodent and human RGCs. Enhancement of axon regeneration following overexpression of miR-19a holds therapeutic potential in human optic neuropathies.

A caution when considering intravitreal injection of miR-19a for axon regeneration is its oncogenic potential. While co-expressing other members of the miR-17-92 cluster may further extend axon outgrowth, overexpression of the miR-17-92 cluster has been impli-

cated in human retinoblastoma, although the oncogenic function in retinoblastoma is not mediated by the miR-19a-PTEN axis.[60] With a selective tropism of AAV2/2 to the inner retina,[61] intravitreal injection of AAV-miR-19a-EGFP attained a high transduction efficiency in RGCs, and we did not observe tumor formation or other abnormal ocular findings in mice intravitreally injected with AAV-miR-19a-EGFP for up to 1 year.

As U6-driven miRNAs are known to induce non-specific transcriptome changes,[62–64] the lack of a scramble control to rule out potential off-targeting effects is a limitation to this study. Furthermore, as there was a total of 76 miRNAs that were differentially expressed in RGCs during development (Figure 1A), modifying the level of miR-19a alone may not be sufficient to recover visual function following optic nerve crush. Modulation of other intrinsic signaling pathways that mediate axon growth capacity, refinement of the extrinsic growth-prohibiting environment, and provision of growth cone
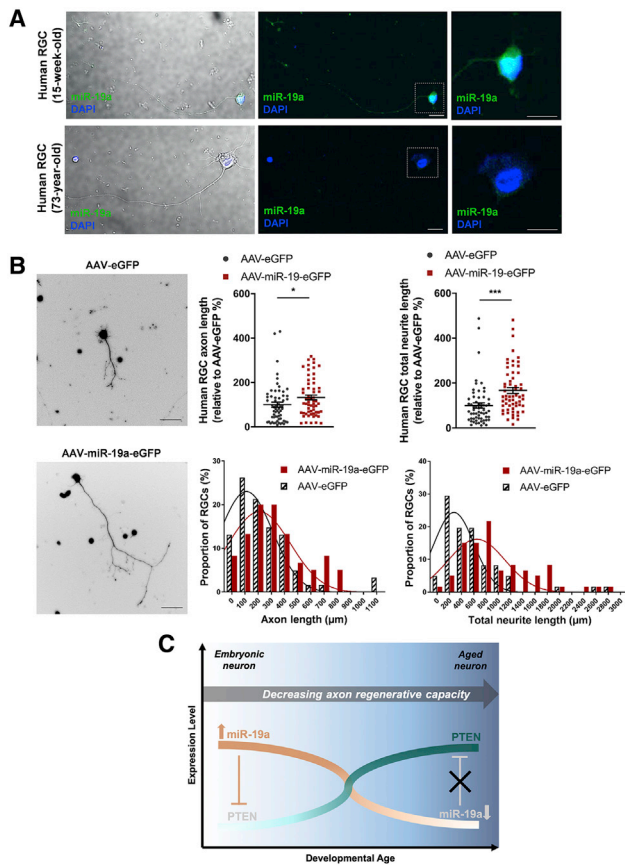
Figure 4. miR-19a Promotes Axon Regeneration in Human Adult RGCs

(A) *In situ* hybridization images of endogenous miR-19a expression (green) in purified fetal (15-week-old) and adult (73-year-old) human RGCs at 7 days *in vitro*. Images on the right are magnifications of boxed areas. miR-19a was most prominently detected in the cytoplasm and decreased in expression from fetal to adult human RGCs. Scale bars, 10 μm. (B) Fluorescence images of purified human adult RGCs transduced with AAV-EGFP or AAV-miR-19a-EGFP (left). Scale bars, 25 μm. Single-cell analysis showed that AAV-miR-19a-EGFP-transduced human adult RGCs (n = 60 RGCs; 2 experimental replicates) had longer axon lengths and total neurite lengths compared with AAV-EGFP-transduced human adult RGCs (n = 61 RGCs; 2 experimental replicates) at 14 days *in vitro* (top) (axon length, p = 0.041; total neurite length, p = 0.0002; total n = 121 RGCs purified from two donors aged 69 years and 75 years). Unpaired two-tailed Student's t test was used for all comparisons; *p < 0.05; ***p < 0.001. All values are shown as mean ± SEM. The proportions of RGCs by axon length and total neurite length between AAV-EGFP-transduced and AAV-miR-19a-EGFP-transduced human RGCs are represented by histograms (bottom). The Gaussian distribution of AAV-EGFP and AAV-miR-19a-EGFP is indicated by an overlapping curve. (C) A schematic illustrating the reciprocal relationship of endogenous expression of miR-19a and PTEN in RGCs during development and their association with the decline in axon regenerative capacity.

guidance cues for synapse formation at the right location would be required to restore the functional integrity of the optic nerve.[65–67]

Although PTEN protein levels significantly increased in P30 RGCs by 60% and 40% from E21 RGCs and from P6 RGCs, respectively (p < 0.001) (Figure 2H), the developmental decline in axon regener-

ative capacity would not be solely accountable by an increase in PTEN expression. Growing evidence suggests that PTEN is not only post-transcriptionally but also post-translationally regulated for regulation of axon growth and regeneration. Post-translational modifications, such as phosphorylation, acetylation, oxidation, *S*-nitrosylation, ubiquitination, or sumoylation, may influence PTEN phosphatase activity, binding to the membrane, subcellular localization, or protein interactions in the regulation of axon growth and regeneration.[68] Antagonizing the PDZ-motif interactions of PTEN using cell-permeable peptides, for example, has been shown to increase neuronal survival, optic nerve regeneration, and visual acuity after optic nerve injury in adult rats.[69]

In summary, our study demonstrates that the miR-19a-PTEN-axis is involved in the developmental decline of axon regenerative capacity in RGCs. That overexpression of miR-19a augments axon regeneration in mature rodent RGCs and aged human RGCs underscores the therapeutic potential of local administration of miRNAs via intravitreal injection to rejuvenate RGCs for axon regeneration in the treatment of optic neuropathies.

MATERIALS AND METHODS
Experimental Design
Sample sizes were determined for each study based on the principle of using the minimum number of animals to provide adequate statistical power, being mindful of the recommendations of the Institutional Animal Care and Use Committee (IACUC) (animal studies). A minimum of three mice were used for each treatment group, according to standard scientific conventions. More mice were used in some experiments to augment statistical power (final n = 5–8 mice per treatment group). Sample size on human biospecimen data was limited by availability. Sample sizes of all other experiments were based on effect sizes and sample-to-sample variability during pilot experiments. Please see below and figure legends for more details.

Data Inclusion and Exclusion
We excluded any data that failed to adhere to criteria that were established prior to data collection. Microfluidic chambers excluded batches with microfluidic chambers that did not fully adhere to culture plates, leading to inconsistent cell density and total cell number. Time-lapse imaging excluded RGCs that were connected to other cells, RGCs without EGFP signal, or RGCs without an extended axon and visible growth cone prior to time-lapse imaging. Our *in vivo* mice model excluded one mouse from the optic nerve count analyses due to an incomplete optic nerve crush (i.e., residual axons remained in optic nerve sections), and another mouse due to retinal hemorrhaging after optic nerve crush, leading to eyeball atrophy before the time of sample retrieval. No other data were excluded from analyses.

Randomization and Blinding
C57BL/6J mice were allocated randomly to receive an intravitreal injection of AAV-miR-19a-EGFP or AAV-EGFP in one eye. All mice in each treatment group were age and sex matched. All manual tracings

of single-cell neurite lengths and microfluidic chamber axon lengths and the counting of regenerated optic nerve axons were analyzed by blinded investigators.

Postmortem Human Retinal Tissues

Human adult retinal tissues were collected from the Hospital Authority Eye Bank, Hong Kong Eye Hospital with written informed consent collected from a closest family member. Human fetal retinal tissues from aborted fetuses were collected from the Department of Obstetrics and Gynecology, Prince of Wales Hospital, Hong Kong, with written informed consent obtained from the mother. All study protocols for human adult and fetal retinal tissues were approved by the Joint CUHK-NTEC Clinical Research Ethics Committee and the Cluster Research Ethics Committee/Institutional Review Board (REC/IRB). Purified RGCs that were cultured for human adult RGC axon growth experiments in this study were collected from retina donors at 69 years (female), 73 years (male), and 75 years (male). There were no known ocular or brain disorders for each donor. Purified human fetal RGCs that were cultured for ISH staining in this study were collected from a fetus at gestation week 14.6.

Experimental Animals

All experimental procedures were approved by The Chinese University of Hong Kong Animal Experimentation Ethics Committee and Hong Kong Department of Health, which adhere to the International Guiding Principles for Biomedical Research Involving Animals and the Hong Kong Code of Practice for Care and Use of Animals for Experimental Purposes. SD rats and C57BL/6J mice were fed standard diet *ad libitum* and housed in a 12-h light/12-h dark light cycle.

Purification of RGCs

RGCs were purified using a magnetic cell sorting technique. Briefly, retinas from SD rats or human donor eyeballs were dissected and dissociated using a neural tissue dissociation kit-postnatal neurons (Miltenyi Biotec, #130-094-802). All retinal tissues were transferred into Neurobasal-A media (Gibco) supplemented with 5% bovine serum albumin (BSA) (Sigma) and placed on ice immediately upon collection. The dissociated retinas were passed through a 40-μm filter (Fisher Scientific) to obtain a single-cell suspension before RGC purification. For rat retinal tissue, primary antibody rat and mouse CD90.1 MicroBeads (Miltenyi Biotec, #130-094-523) and biotinylated depletion antibody (Miltenyi Biotec, #130-096-209) were used for purification of RGCs and depletion of non-RGC neuronal cells, respectively, according to the manufacturer's instructions. For human retinal tissue, primary antibodies human CD90 MicroBeads (Miltenyi Biotec, #130-096-253) and biotinylated human CX3CR1 (clone 2A9-1, Miltenyi Biotec, #130-096-446) were used for purification of RGCs and depletion of non-RGC neuronal cells, respectively. RGCs were eluted from MS columns (Miltenyi Biotec, #130-042-201) using Neurobasal-A media (Gibco) supplemented with $1\times$ B27 (Invitrogen), $1\times$ penicillin/streptomycin (Gibco), 6 mM sodium bicarbonate (Sigma), 1% BSA (Sigma), $1\times$ GlutaMAX (Gibco), 10 ng/mL brain-derived neurotrophic factor (BDNF) (PeproTech), 10 ng/mL ciliary neurotrophic factor (CNTF) (PeproTech), 10 ng/mL insulin-

like growth factor 1 (IGF-1) (PeproTech), and 0.5 μM forskolin (Sigma). Cells were plated at a density of 20–30 cells/mm^2 on culture plates (Corning Life Sciences) pre-coated with 0.2 mg/mL poly-D-lysine (PDL) (Millipore) and 20 μg/mL laminin (Invitrogen). Approximately 30, 20, and 40 retinas from E21, P6, and P30 SD rats, respectively, are required for an average total yield of 8–10 $\times$ 10^5 RGCs.

Rodent RGC Neurite Length Analysis

Images of cultured E21, P6, and P30 RGCs were captured using an inverted Leica DM IRB microscope using the Spot software with a 20$\times$ objective (N Plan L 20$\times$/0.4, Leica) on day 3, 7, and 14 for comparisons of total neurite length. Images were assembled into montages and adjusted for brightness and contrast before manual tracing. Total neurite length was measured using a custom program written in MATLAB (Data S1).

Quantification of Endogenous miRNA in RGCs Using Microarray and TaqMan qRT-PCR

For RNA extraction of purified E21, P6, and P30 RGCs, an RNeasy mini kit (QIAGEN) was used according to the manufacturer's instructions. The quantity (ng/μL) and quality (A_{260}/A_{280}) of the extracted RNA were measured using a spectrophotometer (NanoDrop ND-1000; Thermo Scientific). Three biological replicates were analyzed for E21 (40 retinas per replicate) and P6 (20 retinas per replicate) RGCs. Two biological replicates were analyzed for P30 RGCs (40 retinas per replicate). After RNA extraction, total RNA from E21, P6, and P30 RGCs (100 ng per biological replicate) was used for microarray analysis using a miRNA complete labeling and hybridization kit (Agilent Technologies, #5190-0456) and a SurePrint G3 Rat v16.0 miRNA array kit (Agilent Technologies), according to the manufacturer's instructions. Rat microRNA Microarray v2.0 slides contained probes for 677 rat miRNAs (Sanger miRBase database v16.0). Values from scanned images were extracted using Agilent Feature Extraction software (v9.5.3.1) with the default protocols and settings for background subtraction and signal intensity processing. Non-uniform outliers were excluded. Data were further analyzed using GeneSpring GX software (v11.5). The dataset was normalized using a 75th percentile shift normalization method, which normalizes miRNA expression values of each independent sample to the 75th percentile of the expression intensity across all probes. p values were calculated using a moderated t test with a Benjamini-Hochberg correction.[70–73] For TaqMan qRT-PCR, complementary DNA (cDNA) was synthesized from total RNA using a TaqMan miRNA reverse transcription kit (Applied Biosystems), according to the manufacturer's instructions. TaqMan primer sequences were as follows: miR-17-1-5p, 5′-CAAAGUGCUUACAGUGCAGGUAG-3′; miR-18a-5p, 5′-UAAGGUGCAUCUAGUGCAGAUAG-3′; miR-19a-3p, 5′-UGUGCAAAUCUAUGCAAAACUGA-3′; miR-19b-3p, 5′-UGUGCAAAUCCAUGCAAAACUGA-3′; miR-20a-5p, 5′-UAAAGUGCUUAUAGUGCAGGUAG-3′; miR-92a-3p, 5′-UAUUGCACUUGUCCCGGCCU-GU-3′; and U6 small nuclear RNA (snRNA) (endogenous control), 5′-GTGCTCGCTTCGGCAGCACATATACTAAAATTGGAACGATACAGAGAAGATTAGCATGGCCCCTGCGCAAGGATGAC

ACGCAAATTCGTGAAGCGTTCCATATTTT-3′. Newly synthesized cDNA was qPCR amplified using a TaqMan miRNA assay kit (Applied Biosystems) and Roche PCR machine (LC480 II), according to the manufacturers' instructions. Three biological replicates were assayed per miRNA per PCR reaction (triplicate measurements). Results were averaged across all replicate PCR reactions. The relative gene expression was calculated using the $2^{-\Delta\Delta Ct}$ method[74] with normalization to U6 snRNA and relativity to E21.

Validation of miR-19a Binding onto the PTEN 3′ UTR and Quantification of PTEN Downregulation

For dual luciferase assay, the *PTEN* 3′ UTR was amplified from human cDNA (forward primer, 5′-TAAT**GAGCTC**AATGCTCAGAAAGG AAATAA-3′; reverse primer, 5′-TAAT**TCTAGA**TGCCACAGC AAAGAATGGTG-3′; 2.2-kb length) and contained two miR-19a binding sites; the *SOCS3* 3′ UTR was amplified from human cDNA (forward primer, 5′-TAAT**GAGCTC**ACTCACTGGAGGGCAC-3′; reverse primer, 5′TAAT**TCTAGA**TTTTTCATTAAAAAAT-3′; 0.7-kb length) and contained one miR-19a binding site (upstream SacI and XbaI restriction sites in forward and reverse primers, respectively, are in boldface). Full-length human *PTEN* and the *SOCS3* 3′ UTR contain three and one miR-19a binding sites, respectively. The *PTEN* 3′ UTR with miR-19a binding sites mutated (*mPTEN*) replaced both miR-19a binding sites with AAAAAAA. All three 3′ UTR sequences were cloned into pmirGLO plasmid (Promega) that contained the firefly luciferase (*luc2*) gene as the primary reporter monitoring mRNA regulation, whereas the *Renilla* luciferase (*hRluc-neo*) gene acted as a control reporter for endogenous normalization control (Figures S2A and S2B). DNA plasmids were purified using a QIAfilter Plasmid Midi Kit (QIAGEN). Purified P6 RGCs were cultured at 20–30 cells/mm^2 in 24-well plates (Corning Life Sciences) for 3 days before co-transfection of 0.8 μg of pmirGLO reporter plasmid containing *PTEN*, *mPTEN*, or *SOCS3* 3′ UTRs with 100 nM miR-19a-3p mimic oligonucleotide (mirVana, #4464066) or scramble miRNA oligonucleotide 5′-TAACACGTCTATACGCCCA-3′ (Exiqon, #199006-011) using NeuroMag transfection reagent (1:3; OZ Biosciences). Experiments were performed in four replicates. Firefly and *Renilla* luciferase expression was assayed at 36 h post-transfection using the Dual-Luciferase reporter assay system (Promega), according to the manufacturer's instructions. Luciferase expression was measured using a GloMax 20/20 luminometer (Promega). The relative firefly-to-*Renilla* luciferase ratio was calculated to normalize 3′ UTR expression to endogenous gene expression for each sample. Relative luciferase expression with miRNA targets was relative to luciferase expression with scramble oligonucleotides. Empty vector pmirGLO was used as a positive control for transfection efficiency and signal detection. For immunoblot, purified P6 RGCs were transduced by AAV-miR-19a-EGFP or AAV-EGFP at a multiplicity of infection (MOI) of 1×10^5 and cultured at 40 cells/mm^2. On day 14, RGCs were lysed with radioimmunoprecipitation assay (RIPA) buffer (50 mM Tris-HCl, 150 mM NaCl, 0.1% Triton X-100, 0.5% sodium deoxycholate, 0.1% sodium dodecyl sulfate [SDS], 1 mM sodium orthovanadate, 1 mM NaF, and protease inhibitors [cOmplete, Roche]) for total protein extraction. Concentration of protein was quantified using a total protein assay (Bio-Rad, Hercules, CA, USA). Forty micrograms of protein was used per sample with an

equal volume of 2× Laemmli buffer containing 4% SDS, 10% 2-mercaptoethanol, 20% glycerol, 0.004% bromophenol blue, and 0.125 M Tris-HCl at pH 6.8. For gel electrophoresis and blotting, equal amounts of protein were loaded into a 12.5% acrylamide resolving gel (0.3% bisacrylamide, 0.375 M Tris-HCl, 0.1% SDS, 0.05% ammonium persulfate, and 0.02% tetramethylethylenediamine [TEMED]) and 4% acrylamide stacking gel (0.15% bis-acrylamide, 0.125 M Tris-HCl, 0.1% SDS, 0.05% ammonium persulfate, and 0.02% TEMED). After electrophoresis, the gel was transferred to a nitrocellulose membrane (Amersham Pharmacia, Cleveland, OH, USA) for blotting. Membranes were blocked in 5% non-fat milk powder (Santa Cruz Biotechnology) in Tris-buffered saline with Tween 20 (TBST) buffer at room temperature for 2 h before primary antibody incubation at 4°C overnight with rabbit monoclonal PTEN (1:1,000; Cell Signaling Technology, #9559) or mouse monoclonal SOCS3 (1:1,000; Abcam, #ab14939) diluted in 1% non-fat milk. After incubation, membranes were rinsed and incubated with horseradish peroxidase (HRP)-conjugated secondary antibody (1:1,000; Jackson ImmunoResearch, West Grove, PA, USA) at room temperature for 1 h. GAPDH (1:10,000; Thermo Fisher Scientific, #AM4300) or β-actin (1:10,000; Sigma #A3854) was used as an internal loading control. Chemiluminescent signals from bands were detected using enhanced chemiluminescence (ECL) (Amersham Pharmacia) and imaged using a ChemiDoc CCD camera (Bio-Rad). ImageJ was used to quantify band intensity. All antibodies used in this study can be found in Table S3.

Immunofluorescence Staining

Cultured RGCs were fixed in 4% paraformaldehyde (PFA) for 20 min at room temperature, and retinal whole mounts and optic nerves were fixed in 4% PFA overnight at 4°C before a 5% normal goat serum (The Jackson Laboratory) and 1% BSA (Sigma) solution in PBS was used for blocking. Primary antibodies included rabbit monoclonal BRN3A (1:50; Abcam, #ab81213), rabbit polyclonal GAP43 (1:200; Abcam, #ab12274), mouse monoclonal MAP2 (1:200; Upstate Biotechnology, #05-346), rabbit monoclonal PTEN (1:100; Cell Signaling Technology, #9559), rabbit monoclonal TAU (1:200; Abcam, #ab32057), and mouse monoclonal TUJ1 (1:200; Millipore, #MAB5564). Primary antibodies were diluted using 2% normal goat serum (NGS) and 1% BSA in PBS (0.03% Triton X-100 was supplemented for BRN3A) and incubated overnight at 4°C. Secondary antibodies were diluted 1:500 (Alexa Fluor 488 or Alexa Fluor 555 conjugates; Molecular Probes, Thermo Fisher Scientific) with Hoechst (1:1,000; Sigma, #H6024) using 2% NGS and 1% BSA in PBS at room temperature (2 h). Coverslips or slides were mounted using GB-Mount (GBI Labs). Images were captured using a Nikon A1MP confocal microscope using the NIS-Elements software with a 40× objective (NIR Apo 40 x/0.8W, Nikon), or a Nikon Eclipse Ti microscope using the NIS-Elements software with a 20× objective (S Plan Fluor 20×, Nikon).

ISH of miR-19a in Human and Rodent Purified RGCs and Rodent Retinas

A miRNA ISH optimization kit (Exiqon) and TSA plus fluorescein evaluation kit (PerkinElmer) were used for chromogenic and fluorescent detection of miR-19a in the retinas and cultured RGCs,

respectively, according to the manufacturer's instructions. Retinas were fixed in 4% PFA at 4°C overnight, cryoprotected in serial dilutions of sucrose (5%, 15%, and 30%), and snap-frozen in Tissue-Tek optimal cutting temperature (OCT) compound (Fisher Scientific). Only cryosections (8 μm) containing both pupil and optic nerve structures were examined. Before probe hybridization, cryosections were heated at 40°C for 20 min before OCT compound removal by PBS. Purified RGCs cultured on 13-mm coverslips (Marienfeld, Germany) for 7 days were fixed using 4% PFA at room temperature for 20 min before fluorescent ISH detection. Double digoxigenin (DIG)-labeled miRCURY locked nucleic acid (LNA) miRNA detection probes (Exiqon) included the following: miR-19a-3p, 5′-TC AGTTTTGCATAGATTTGCAC-3′ (40 nM; Exiqon, #611510-360); scramble miRNA negative control, 5′-GTGTAACACGTCTATA CGCCCA-3′ (40 nM; Exiqon, #699004-360); and U6 snRNA positive control, 5′-CACGAATTTGCGTGTCATCCTT-3′ (4 nM; Exiqon, #699002-360). All procedures before the addition of primary antibody were the same for chromogenic and fluorescent ISH. Primary antibodies used for chromogenic and fluorescent ISH were anti-DIG-AP (1:800; Roche) and anti-DIG-POD (1:800; Roche), respectively. Samples were mounted with GB-Mount (GBI Labs) after counterstaining with Hoechst (1:1,000; Sigma, #H6024). For fluorescent samples, images were captured using a Nikon A1MP confocal microscope using the NIS-Elements software with a 40× objective (NIR Apo 40×/0.8W, Nikon). For chromogenic samples, images were captured using an upright Carl Zeiss Axioplan 2 microscope using the Spot software with a 20× objective (Plan-Apochromat 20×/0.75, Carl Zeiss).

AAV Design and Packaging

AAV-miR-19a-EGFP was packaged by Virovek (Hayward, CA, USA). Mature miR-19a-3p sequence 5′-TCAGTTTTGCATA-GATTTGCACA-3′ was cloned into a pFastBac (pFB) AAV2/2 shuttle vector with a hybrid construct consisting of the cytomegalovirus (CMV) enhancer fused to the chicken β-actin promoter (CAG) promoter and an EGFP fluorescent marker. An empty vector control without a miRNA insert was cloned using the same backbone with either EGFP (green) or mCherry (red) as a fluorescent marker (Figure S3A). Validation with TaqMan qRT-PCR demonstrated a 2.5 ± 0.3-fold increase of miR-19a expression levels in RGCs transduced with AAV-miR-19a-EGFP compared with those transduced with an AAV-EGFP empty vector control (Figure S3C). AAV-miR-19aTuD-EGFP was packaged by the University of Iowa, Viral Vector Core (Iowa City, IA, USA). The miR-19aTuD sequence 5′-GGATC CGACGGCGCTAGGATCATCAAC*CAGTTTT*ccca*ATAGA*TTTGC ACACAAGTATTCTGGTCACAGAATACAAC*CAGTTTT*ccca*ATA GATTTGCACA*CAAGATGATCCTAGCGCCGTCTTTTTTGAAT TC-3′ (binding site of miR-19a is italicized, seed sequence is underlined, and lowercase letters indicate location of induced bulge to increase miRNA binding affinity by imperfect complementarity) was designed based on previously described methods of AAV-mediated expression of miRNA TuD constructs[59] and cloned into a pFB AAV2/2 shuttle vector with a CMV promoter and an EGFP fluorescent marker (Figures S3A and S3B). An empty vector control was cloned using the same backbone with an EGFP fluorescent marker. Validation with TaqMan qRT-PCR demonstrated a 74% ± 9.9% reduction in miR-19a expression levels in RGCs transduced with AAV-miR-19aTuD-EGFP compared with those transduced with AAV-EGFP empty vector control (Figure S3C). All RGCs in vitro were transduced at an MOI of 1×10^5 viral genomes (vg)/cell.

RGC Culture in Microfluidic Chamber

Axon length was measured by plating purified P6 RGCs into a microfluidic chamber device (Xona Microfluidics, #RD450) (Figure S4A) for the separation of RGC soma and dendrites from axons (Figures S4B and S4C). The device is composed of two compartments joined by microgrooves that extend 450 μm from one compartment to the other. With RGC somas and dendrites localized in one compartment, only axons extended into the adjacent compartment through microgrooves. Purified P6 RGCs were transduced by AAV-miR-19a-EGFP or AAV-EGFP at an MOI of 1×10^5 and plated at a density of 3–4 × 10^5 cells/chamber. Images were captured and automatically stitched using a Nikon Eclipse Ti microscope and NIS-Elements software on day 14 using a 20× objective (S Plan Fluor 20×, Nikon). All axons extended into the axon compartment were manually traced before measurement of total axon length (i.e., sum of all manually traced axon extensions) using a custom program written in MATLAB (Data S2).

Time-Lapse Imaging of RGCs

The rate of axon extension of purified RGCs (cultured at 20 cells/mm²) from P6 SD rats transduced by AAV-miR-19a-EGFP or AAV-EGFP (MOI of 1×10^5) was measured with time-lapse imaging. RGCs cultured for 14 days were trypsinized and replated onto glass-bottom dishes (MatTek, #P35G-1.0-14) pre-coated with 0.2 mg/mL PDL (Millipore) and 20 μg/mL laminin (Invitrogen) in a 37°C heated chamber (Chamlide UM, Live Cell Instrument, Korea) with 5% CO_2. Only RGCs with EGFP expression and an extended neurite with a visible growth cone were selected for time-lapse imaging. Images were automatically captured every 20 min for 8 h by a Nikon A1MP confocal microscope using the NIS-Elements software with a 40× objective (NIR Apo 40×/0.8W, Nikon). The longest neurite length and soma area were manually traced and measured at each time point using the NIS-Elements analysis software (NIS AR, Nikon). Circularity was defined as $4\pi a/p^2$, where *a* and *p* represent the area and perimeter of a cell, respectively. Circularity equals 1 for circles, whereas all other shapes have a circularity less than 1 (NIS AR, Nikon).

Intravitreal Injection of AAV and Optic Nerve Crush

Sixteen 1-month-old C57BL/6J mice (males) were anaesthetized with 100 mg/kg ketamine and 9 mg/kg xylazine. Intravitreal injection of 1 μL (2.13×10^{13} vg/mL) of AAV-miR-19a-EGFP (n = 8 mice) or AAV-EGFP (n = 8 mice) was performed in one eye of each animal. The optic nerve of the injected eye was crushed 3–4 weeks after the intravitreal injection. After anaesthetizing the animals (as described above), inferior limbal conjunctival peritomy was performed. The conjunctiva was gently peeled back to allow access to the retrobulbar

region. The optic nerve was exposed through a small window after a gentle blunt dissection dissociating the surrounding blood sinuses and connective tissue. The optic nerve was crushed using a pair of Dumant no. 5 self-closing tweezers (Ted Pella, Redding, CA, USA) for 2 s at a site approximately 1 mm posterior to the globe. Antibiotic ointment was applied to the surgical site after injection. During the postoperative period, mice were monitored for normal eating and drinking behavior.

Quantification of Regenerated Axons in the Optic Nerve

After 3–4 weeks of optic nerve crush, mice were anesthetized with 100 mg/kg ketamine and 9 mg/kg xylazine. The eye with optic nerve crush received intravitreal injection of 1 μL of CTB Alexa Fluor 555 conjugate (2 μg/μL; Invitrogen). Four days after intravitreal injection of CTB, mice were perfused using 4% PFA. The eyeballs were removed and immersed in 4% PFA at 4°C overnight for TUJ1 staining (see Immunofluorescence Staining for Quantification of RGC Survival). The optic nerves were dissected, immersed in 4% PFA at 4°C overnight, cryoprotected in serial dilutions of sucrose (5%, 15%, and 30%), and snap-frozen in Tissue-Tek OCT compound (Fisher Scientific). The cryosections were cut at 8-μm thickness (t) using a cryostat (CryoStar NX50, Thermo Scientific). Three to five sections of each optic nerve were used for analysis by two blinded observers. The numbers of CTB-labeled axons were counted at distances of 0.2, 0.5, 1, 1.5, 2, 2.5, 3, 3.5, and 4 mm from the optic nerve crush site. The cross-sectional width of the optic nerve was measured at every recorded distance from the optic nerve crush site. The radius (r) (μm) of the optic nerve at every recorded distance was defined as the measured width (w) (μm) divided by 2. The total number of regenerated axons (a) at every recorded distance (d) (mm) from the optic nerve crush site was estimated by averaging all sections with r (μm), w (μm), and t (μm) as follows: $a_d = \pi r^2 \times$ [average number of counted regenerated axons per section per recorded distance/$(w \times t)$].

Immunofluorescence Staining for Quantification of RGC Survival

Retinas were dissected for TUJ1 immunofluorescence staining to quantify the number of surviving RGCs after optic nerve crush. Retinas were blocked in 5% NGS and 1% BSA for 1 h at room temperature and incubated with monoclonal TUJ1 antibody (1:500; Covance, #PRB-425P) in 2% NGS and 1% BSA overnight at 4°C. Anti-rabbit secondary antibody (Alexa Fluor 350, Thermo Fisher Scientific) was used in 2% NGS and 1% BSA at 1:500 for 2 h at room temperature. Retinas were flat-mounted with the RGC layer facing upward and mounted onto a glass slide using GB-Mount (GBI Labs). Images were captured with a Nikon A1MP confocal microscope using the NIS-Elements software with a 40× objective (NIR Apo 40×/0.8W, Nikon). A total of 24 fields were imaged per retina (6 fields per retinal quadrant). The total number of TUJ1-positive cells per field was measured across all images per eye.

Human RGC Axon and Neurite Length Analysis

Purified human adult RGCs were plated at 40 cells/mm² and transduced with either AAV-EGFP or AAV-miR-19a-EGFP at an MOI of 1 × 10⁵. Two weeks post-transduction, RGCs were fixed and

imaged using a Nikon Eclipse Ti microscope using the NIS-Elements software with a 20× objective (S Plan Fluor 20×, Nikon). Only RGCs with EGFP expression were included for analysis. All RGC cell bodies and neurites were manually traced before axon length and total neurite length analysis using a written MATLAB program (Data S1). The longest neurite of the RGC was identified as the axon.

Statistical Analysis

Statistical analyses were performed using Stata 13.0 (StataCorp, College Station, TX, USA). A two-tailed moderated t test with a Benjamini-Hochberg correction for false discovery rate was used to compare the means of miRNA microarray expression values between E21 and P6 and between E21 and P30.[70–73] An unpaired two-tailed Student's t test was used for comparisons between two groups of equal sample size: (1) miR-17-92 expression levels measured by TaqMan qRT-PCR between E21 and P6/P30 RGCs; (2) RGC neurite lengths *in vitro* between E21 and P6/P30 RGCs; (3) dual luciferase *PTEN, mPTEN,* and *SOCS3* 3′ UTR expression levels between scramble oligos and miR-19a mimic oligos; (4) miR-19a fold change measured by TaqMan qRT-PCR between AAV-EGFP- and AAV-miR-19a-EGFP-transduced RGCs and between AAV-EGFP- and AAV-miR-19aTuD-EGFP-transduced RGCs; (5) PTEN and SOCS3 immunoblots between AAV-EGFP- and AAV-miR-19a-EGFP-transduced RGCs; (6) immunocytofluorescent staining of PTEN between AAV-EGFP- and AAV-miR-19a-EGFP-transduced RGCs and between AAV-EGFP- and AAV-miR-19aTuD-EGFP-transduced RGCs; (7) immunocytofluorescent staining of PTEN between E21 and P6, E21 and P30, and P6 and P30 RGCs; (8) microfluidic chamber axon lengths between AAV-EGFP- and AAV-miR-19a-EGFP-transduced RGCs and between AAV-EGFP- and AAV-miR-19aTuD-EGFP-transduced RGCs; (9) RGC soma diameter, soma circularity, duration, baseline length, and length of axon extension between AAV-EGFP- and AAV-miR-19a-EGFP-transduced RGCs; (10) TUJ1-positive RGCs after optic nerve crush between AAV-EGFP- and AAV-miR-19a-EGFP-transduced retinas; and (11) human RGC axon lengths and total neurite lengths between AAV-EGFP- and AAV-miR-19a-EGFP-transduced RGCs. Multivariable linear mixed modeling was used for analysis of (1) time-lapse imaging comparing the rates of axon extension between AAV-EGFP- and AAV-miR-19a-EGFP-transduced RGCs and (2) optic nerve count of regenerated axonal fibers, controlling for repeated measurements. For time-lapse imaging for measurement of axon extension, the model was fitted with axon length as the dependent variable; time, types of AAV transduction (AAV-EGFP or AAV-miR-19a-EGFP), the interaction between time and types of AAV transduction (to determine whether the types of AAV transduction would affect the rate of axon extension), baseline axon length, and the interaction between baseline axon length and time served as fixed effects variables, including random intercepts (axon lengths measured at multiple time points nested within cell) and random coefficients for time for individual RGCs. For optic nerve counts, the model was fitted with CTB-labeled axon length as the dependent variable; distance from optic nerve crush site and types of AAV transduction (AAV-EGFP or AAV-miR-19a-EGFP) served as fixed effects variables, with random intercepts for individual

mice (number of CTB-labeled axons nested within mice). In all analyses, p <0.05 was considered to be statistically significant.

Data and Software Availability
All microarray data that support the findings of this study have been deposited in the National Center for Biotechnology Information Gene Expression Omnibus (GEO: GSE102458). All other relevant data are available from the corresponding author upon request. All MATLAB software coding that support the findings of this study are provided in Supplemental Information.

SUPPLEMENTAL INFORMATION
Supplemental Information can be found online at https://doi.org/10.1016/j.omtn.2020.05.031.

AUTHOR CONTRIBUTIONS
J.S.Y.Y. assisted with cell culture, immunoblotting, and luciferase plasmid designs. X.C. assisted with cell culture and neurite imaging and tracing. S.H.N. assisted with optic nerve crush and performed sample retrieval and optic nerve sectioning and imaging. K.W.C. and C.C.W. provided fetal retinal tissue samples and performed the microarray. T.K.N. and T.Y.C.H. assisted with purification of RGCs and data analyses. H.K.M. performed all other experiments, data analyses, data interpretation, and wrote the manuscript. W.K.C., T.L.L., T.K.N., R.N.W., and W.H.Y. contributed to the design of the study and proofing of the manuscript. C.K.L. conceived and designed the study, performed intravitreal injections and optic nerve crush, assisted with data analysis and interpretation, supervised the work, wrote the manuscript, and gave final approval of the manuscript.

CONFLICTS OF INTEREST
The authors declare no competing interests.

REFERENCES
1. Goldberg, J.L., Klassen, M.P., Hua, Y., and Barres, B.A. (2002). Amacrine-signaled loss of intrinsic axon growth ability by retinal ganglion cells. Science 296, 1860–1864.

2. Goldberg, J.L., Espinosa, J.S., Xu, Y., Davidson, N., Kovacs, G.T.A., and Barres, B.A. (2002). Retinal ganglion cells do not extend axons by default: promotion by neurotrophic signaling and electrical activity. Neuron 33, 689–702.

3. McKerracher, L., David, S., Jackson, D.L., Kottis, V., Dunn, R.J., and Braun, P.E. (1994). Identification of myelin-associated glycoprotein as a major myelin-derived inhibitor of neurite growth. Neuron 13, 805–811.

4. Mukhopadhyay, G., Doherty, P., Walsh, F.S., Crocker, P.R., and Filbin, M.T. (1994). A novel role for myelin-associated glycoprotein as an inhibitor of axonal regeneration. Neuron 13, 757–767.

5. Huber, A.B., and Schwab, M.E. (2000). Nogo-A, a potent inhibitor of neurite outgrowth and regeneration. Biol. Chem. 381, 407–419.

6. Snow, D.M., and Letourneau, P.C. (1992). Neurite outgrowth on a step gradient of chondroitin sulfate proteoglycan (CS-PG). J. Neurobiol. 23, 322–336.

7. Bradbury, E.J., Moon, L.D.F., Popat, R.J., King, V.R., Bennett, G.S., Patel, P.N., Fawcett, J.W., and McMahon, S.B. (2002). Chondroitinase ABC promotes functional recovery after spinal cord injury. Nature 416, 636–640.

8. Huang, J.K., Phillips, G.R., Roth, A.D., Pedraza, L., Shan, W., Belkaid, W., Mi, S., Fex-Svenningsen, A., Florens, L., Yates, J.R., 3rd, and Colman, D.R. (2005). Glial membranes at the node of Ranvier prevent neurite outgrowth. Science 310, 1813–1817.

9. Cai, D., Shen, Y., De Bellard, M., Tang, S., and Filbin, M.T. (1999). Prior exposure to neurotrophins blocks inhibition of axonal regeneration by MAG and myelin via a cAMP-dependent mechanism. Neuron 22, 89–101.

10. Cai, D., Qiu, J., Cao, Z., McAtee, M., Bregman, B.S., and Filbin, M.T. (2001). Neuronal cyclic AMP controls the developmental loss in ability of axons to regenerate. J. Neurosci. 21, 4731–4739.

11. Song, H., Ming, G., He, Z., Lehmann, M., McKerracher, L., Tessier-Lavigne, M., and Poo, M. (1998). Conversion of neuronal growth cone responses from repulsion to attraction by cyclic nucleotides. Science 281, 1515–1518.

12. Neumann, S., and Woolf, C.J. (1999). Regeneration of dorsal column fibers into and beyond the lesion site following adult spinal cord injury. Neuron 23, 83–91.

13. Gao, Y., Deng, K., Hou, J., Bryson, J.B., Barco, A., Nikulina, E., Spencer, T., Mellado, W., Kandel, E.R., and Filbin, M.T. (2004). Activated CREB is sufficient to overcome inhibitors in myelin and promote spinal axon regeneration in vivo. Neuron 44, 609–621.

14. Park, K.K., Liu, K., Hu, Y., Smith, P.D., Wang, C., Cai, B., Xu, B., Connolly, L., Kramvis, I., Sahin, M., and He, Z. (2008). Promoting axon regeneration in the adult CNS by modulation of the PTEN/mTOR pathway. Science 322, 963–966.

15. Moore, D.L., Blackmore, M.G., Hu, Y., Kaestner, K.H., Bixby, J.L., Lemmon, V.P., and Goldberg, J.L. (2009). KLF family members regulate intrinsic axon regeneration ability. Science 326, 298–301.

16. Smith, P.D., Sun, F., Park, K.K., Cai, B., Wang, C., Kuwako, K., Martinez-Carrasco, I., Connolly, L., and He, Z. (2009). SOCS3 deletion promotes optic nerve regeneration in vivo. Neuron 64, 617–623.

17. Sun, F., Park, K.K., Belin, S., Wang, D., Lu, T., Chen, G., Zhang, K., Yeung, C., Feng, G., Yankner, B.A., and He, Z. (2011). Sustained axon regeneration induced by co-deletion of PTEN and SOCS3. Nature 480, 372–375.

18. Welsbie, D.S., Yang, Z., Ge, Y., Mitchell, K.L., Zhou, X., Martin, S.E., Berlinicke, C.A., Hackler, L., Jr., Fuller, J., Fu, J., et al. (2013). Functional genomic screening identifies dual leucine zipper kinase as a key mediator of retinal ganglion cell death. Proc. Natl. Acad. Sci. USA 110, 4045–4050.

19. Duan, X., Qiao, M., Bei, F., Kim, I.J., He, Z., and Sanes, J.R. (2015). Subtype-specific regeneration of retinal ganglion cells following axotomy: effects of osteopontin and mTOR signaling. Neuron 85, 1244–1256.

20. Norsworthy, M.W., Bei, F., Kawaguchi, R., Wang, Q., Tran, N.M., Li, Y., Brommer, B., Zhang, Y., Wang, C., Sanes, J.R., et al. (2017). Sox11 expression promotes regeneration of some retinal Ganglion cell types but kills others. Neuron 94, 1112–1120.e4.

21. Bartel, D.P. (2004). MicroRNAs: genomics, biogenesis, mechanism, and function. Cell 116, 281–297.

22. Lagos-Quintana, M., Rauhut, R., Meyer, J., Borkhardt, A., and Tuschl, T. (2003). New microRNAs from mouse and human. RNA 9, 175–179.

23. Bernstein, E., Kim, S.Y., Carmell, M.A., Murchison, E.P., Alcorn, H., Li, M.Z., Mills, A.A., Elledge, S.J., Anderson, K.V., and Hannon, G.J. (2003). Dicer is essential for mouse development. Nat. Genet. 35, 215–217.

24. Christensen, M., and Schratt, G.M. (2009). MicroRNA involvement in developmental and functional aspects of the nervous system and in neurological diseases. Neurosci. Lett. 466, 55–62.

25. Johnston, R.J., and Hobert, O. (2003). A microRNA controlling left/right neuronal asymmetry in Caenorhabditis elegans. Nature 426, 845–849.

26. Chang, S., Johnston, R.J., Jr., Frøkjaer-Jensen, C., Lockery, S., and Hobert, O. (2004). MicroRNAs act sequentially and asymmetrically to control chemosensory laterality in the nematode. Nature 430, 785–789.

27. Hsieh, Y.-W., Chang, C., and Chuang, C.-F. (2012). The microRNA *mir-71* inhibits calcium signaling by targeting the TIR-1/Sarm1 adaptor protein to control stochastic L/R neuronal asymmetry in *C. elegans*. PLoS Genet. *8*, e1002864.

28. Davis, T.H., Cuellar, T.L., Koch, S.M., Barker, A.J., Harfe, B.D., McManus, M.T., and Ullian, E.M. (2008). Conditional loss of Dicer disrupts cellular and tissue morphogenesis in the cortex and hippocampus. J. Neurosci. *28*, 4322–4330.

29. Damiani, D., Alexander, J.J., O'Rourke, J.R., McManus, M., Jadhav, A.P., Cepko, C.L., Hauswirth, W.W., Harfe, B.D., and Strettoi, E. (2008). Dicer inactivation leads to progressive functional and structural degeneration of the mouse retina. J. Neurosci. *28*, 4878–4887.

30. Krichevsky, A.M., Sonntag, K.-C., Isacson, O., and Kosik, K.S. (2006). Specific microRNAs modulate embryonic stem cell-derived neurogenesis. Stem Cells *24*, 857–864.

31. Sasaki, Y., Gross, C., Xing, L., Goshima, Y., and Bassell, G.J. (2014). Identification of axon-enriched microRNAs localized to growth cones of cortical neurons. Dev. Neurobiol. *74*, 397–406.

32. Zhang, Y., Ueno, Y., Liu, X.S., Buller, B., Wang, X., Chopp, M., and Zhang, Z.G. (2013). The MicroRNA-17-92 cluster enhances axonal outgrowth in embryonic cortical neurons. J. Neurosci. *33*, 6885–6894.

33. Dajas-Bailador, F., Bonev, B., Garcez, P., Stanley, P., Guillemot, F., and Papalopulu, N. (2012). MicroRNA-9 regulates axon extension and branching by targeting Map1b in mouse cortical neurons. Nat. Neurosci. *15*, 697–699.

34. Lewis, B.P., Shih, I.-H., Jones-Rhoades, M.W., Bartel, D.P., and Burge, C.B. (2003). Prediction of mammalian microRNA targets. Cell *115*, 787–798.

35. Pezzolesi, M.G., Platzer, P., Waite, K.A., and Eng, C. (2008). Differential expression of *PTEN*-targeting microRNAs *miR-19a* and *miR-21* in Cowden syndrome. Am. J. Hum. Genet. *82*, 1141–1149.

36. Dou, L., Meng, X., Sui, X., Wang, S., Shen, T., Huang, X., Guo, J., Fang, W., Man, Y., Xi, J., and Li, J. (2015). miR-19a regulates PTEN expression to mediate glycogen synthesis in hepatocytes. Sci. Rep. *5*, 11602.

37. Magill, S.T., Cambronne, X.A., Luikart, B.W., Lioy, D.T., Leighton, B.H., Westbrook, G.L., Mandel, G., and Goodman, R.H. (2010). MicroRNA-132 regulates dendritic growth and arborization of newborn neurons in the adult hippocampus. Proc. Natl. Acad. Sci. USA *107*, 20382–20387.

38. Heyer, M.P., Pani, A.K., Smeyne, R.J., Kenny, P.J., and Feng, G. (2012). Normal midbrain dopaminergic neuron development and function in miR-133b mutant mice. J. Neurosci. *32*, 10887–10894.

39. Lehmann, S.M., Krüger, C., Park, B., Derkow, K., Rosenberger, K., Baumgart, J., Trimbuch, T., Eom, G., Hinz, M., Kaul, D., et al. (2012). An unconventional role for miRNA: let-7 activates Toll-like receptor 7 and causes neurodegeneration. Nat. Neurosci. *15*, 827–835.

40. La Torre, A., Georgi, S., and Reh, T.A. (2013). Conserved microRNA pathway regulates developmental timing of retinal neurogenesis. Proc. Natl. Acad. Sci. USA *110*, E2362–E2370.

41. Hancock, M.L., Preitner, N., Quan, J., and Flanagan, J.G. (2014). MicroRNA-132 is enriched in developing axons, locally regulates Rasa1 mRNA, and promotes axon extension. J. Neurosci. *34*, 66–78.

42. Han, J., Kim, H.J., Schafer, S.T., Paquola, A., Clemenson, G.D., Toda, T., Oh, J., Pankonin, A.R., Lee, B.S., Johnston, S.T., et al. (2016). Functional implications of miR-19 in the migration of newborn neurons in the adult brain. Neuron *91*, 79–89.

43. Concepcion, C.P., Bonetti, C., and Ventura, A. (2012). The microRNA-17-92 family of microRNA clusters in development and disease. Cancer J. *18*, 262–267.

44. Mi, H., Huang, X., Muruganujan, A., Tang, H., Mills, C., Kang, D., and Thomas, P.D. (2017). PANTHER version 11: expanded annotation data from Gene Ontology and Reactome pathways, and data analysis tool enhancements. Nucleic Acids Res. *45* (D1), D183–D189.

45. Shibata, M., Ishii, J., Koizumi, H., Shibata, N., Dohmae, N., Takio, K., Adachi, H., Tsujimoto, M., and Arai, H. (2004). Type F scavenger receptor SREC-I interacts with advillin, a member of the gelsolin/villin family, and induces neurite-like outgrowth. J. Biol. Chem. *279*, 40084–40090.

46. Thomas, G.M., and Huganir, R.L. (2004). MAPK cascade signalling and synaptic plasticity. Nat. Rev. Neurosci. *5*, 173–183.

47. Hata, K., Fujitani, M., Yasuda, Y., Doya, H., Saito, T., Yamagishi, S., Mueller, B.K., and Yamashita, T. (2006). RGMa inhibition promotes axonal growth and recovery after spinal cord injury. J. Cell Biol. *173*, 47–58.

48. Toth, C., Shim, S.Y., Wang, J., Jiang, Y., Neumayer, G., Belzil, C., Liu, W.Q., Martinez, J., Zochodne, D., and Nguyen, M.D. (2008). Ndel1 promotes axon regeneration via intermediate filaments. PLoS ONE *3*, e2014.

49. Goldshmit, Y., Spanevello, M.D., Tajouri, S., Li, L., Rogers, F., Pearse, M., Galea, M., Bartlett, P.F., Boyd, A.W., and Turnley, A.M. (2011). EphA4 blockers promote axonal regeneration and functional recovery following spinal cord injury in mice. PLoS ONE *6*, e24636.

50. Shigyo, M., Kuboyama, T., Sawai, Y., Tada-Umezaki, M., and Tohda, C. (2015). Extracellular vimentin interacts with insulin-like growth factor 1 receptor to promote axonal growth. Sci. Rep. *5*, 12055.

51. Grimson, A., Farh, K.K.-H., Johnston, W.K., Garrett-Engele, P., Lim, L.P., and Bartel, D.P. (2007). MicroRNA targeting specificity in mammals: determinants beyond seed pairing. Mol. Cell *27*, 91–105.

52. Agarwal, V., Bell, G.W., Nam, J.-W., and Bartel, D.P. (2015). Predicting effective microRNA target sites in mammalian mRNAs. eLife *4*, e05005.

53. Sarbassov, D.D., Guertin, D.A., Ali, S.M., and Sabatini, D.M. (2005). Phosphorylation and regulation of Akt/PKB by the rictor-mTOR complex. Science *307*, 1098–1101.

54. Dowling, R.J.O., Topisirovic, I., Alain, T., Bidinosti, M., Fonseca, B.D., Petroulakis, E., Wang, X., Larsson, O., Selvaraj, A., Liu, Y., et al. (2010). mTORC1-mediated cell proliferation, but not cell growth, controlled by the 4E-BPs. Science *328*, 1172–1176.

55. Hsu, P.P., Kang, S.A., Rameseder, J., Zhang, Y., Ottina, K.A., Lim, D., Peterson, T.R., Choi, Y., Gray, N.S., Yaffe, M.B., et al. (2011). The mTOR-regulated phosphoproteome reveals a mechanism of mTORC1-mediated inhibition of growth factor signaling. Science *332*, 1317–1322.

56. Hsieh, A.C., Liu, Y., Edlind, M.P., Ingolia, N.T., Janes, M.R., Sher, A., Shi, E.Y., Stumpf, C.R., Christensen, C., Bonham, M.J., et al. (2012). The translational landscape of mTOR signalling steers cancer initiation and metastasis. Nature *485*, 55–61.

57. Thoreen, C.C., Chantranupong, L., Keys, H.R., Wang, T., Gray, N.S., and Sabatini, D.M. (2012). A unifying model for mTORC1-mediated regulation of mRNA translation. Nature *485*, 109–113.

58. Mori, S., Nada, S., Kimura, H., Tajima, S., Takahashi, Y., Kitamura, A., Oneyama, C., and Okada, M. (2014). The mTOR pathway controls cell proliferation by regulating the FoxO3a transcription factor via SGK1 kinase. PLoS ONE *9*, e88891.

59. Xie, J., Ameres, S.L., Friedline, R., Hung, J.-H., Zhang, Y., Xie, Q., Zhong, L., Su, Q., He, R., Li, M., et al. (2012). Long-term, efficient inhibition of microRNA function in mice using rAAV vectors. Nat. Methods *9*, 403–409.

60. Conkrite, K., Sundby, M., Mukai, S., Thomson, J.M., Mu, D., Hammond, S.M., and MacPherson, D. (2011). miR-17∼92 cooperates with RB pathway mutations to promote retinoblastoma. Genes Dev. *25*, 1734–1745.

61. Cao, X., Yung, J., Mak, H., and Leung, C.K.S. (2019). Factors governing the transduction efficiency of adeno-associated virus in the retinal ganglion cells following intravitreal injection. Gene Ther. *26*, 109–120.

62. Grimm, D., Streetz, K.L., Jopling, C.L., Storm, T.A., Pandey, K., Davis, C.R., Marion, P., Salazar, F., and Kay, M.A. (2006). Fatality in mice due to oversaturation of cellular microRNA/short hairpin RNA pathways. Nature *441*, 537–541.

63. Giering, J.C., Grimm, D., Storm, T.A., and Kay, M.A. (2008). Expression of shRNA from a tissue-specific pol II promoter is an effective and safe RNAi therapeutic. Mol. Ther. *16*, 1630–1636.

64. Jackson, A.L., and Linsley, P.S. (2004). Noise amidst the silence: off-target effects of siRNAs? Trends Genet. *20*, 521–524.

65. de Lima, S., Koriyama, Y., Kurimoto, T., Oliveira, J.T., Yin, Y., Li, Y., Gilbert, H.Y., Fagiolini, M., Martinez, A.M., and Benowitz, L. (2012). Full-length axon regeneration in the adult mouse optic nerve and partial recovery of simple visual behaviors. Proc. Natl. Acad. Sci. USA *109*, 9149–9154.

66. Lim, J.-H.A., Stafford, B.K., Nguyen, P.L., Lien, B.V., Wang, C., Zukor, K., He, Z., and Huberman, A.D. (2016). Neural activity promotes long-distance, target-specific regeneration of adult retinal axons. Nat. Neurosci. *19*, 1073–1084.

67. Benowitz, L.I., He, Z., and Goldberg, J.L. (2017). Reaching the brain: advances in optic nerve regeneration. Exp. Neurol. *287*, 365–373.

68. Kreis, P., Leondaritis, G., Lieberam, I., and Eickholt, B.J. (2014). Subcellular targeting and dynamic regulation of PTEN: implications for neuronal cells and neurological disorders. Front. Mol. Neurosci. *7*, 23.

69. Shabanzadeh, A.P., D'Onofrio, P.M., Magharious, M., Choi, K.A.B., Monnier, P.P., and Koeberle, P.D. (2019). Modifying PTEN recruitment promotes neuron survival, regeneration, and functional recovery after CNS injury. Cell Death Dis. *10*, 567.

70. Benjamini, Y., and Hochberg, Y. (1995). Controlling the false discovery rate: a practical and powerful approach to multiple testing. J. R. Stat. Soc. B *57*, 289–300.

71. Benjamini, Y., and Yekutieli, D. (2001). The control of the false discovery rate in multiple testing under dependency. Ann. Stat. *29*, 1165–1188.

72. Smyth, G.K. (2004). Linear models and empirical Bayes methods for assessing differential expression in microarray experiments. Stat. Appl. Genet. Mol. Biol. *3*, Article3.

73. Wang, H., Ach, R.A., and Curry, B. (2007). Direct and sensitive miRNA profiling from low-input total RNA. RNA *13*, 151–159.

74. Livak, K.J., and Schmittgen, T.D. (2001). Analysis of relative gene expression data using real-time quantitative PCR and the $2^{-\Delta\Delta C(T)}$ method. Methods *25*, 402–408.
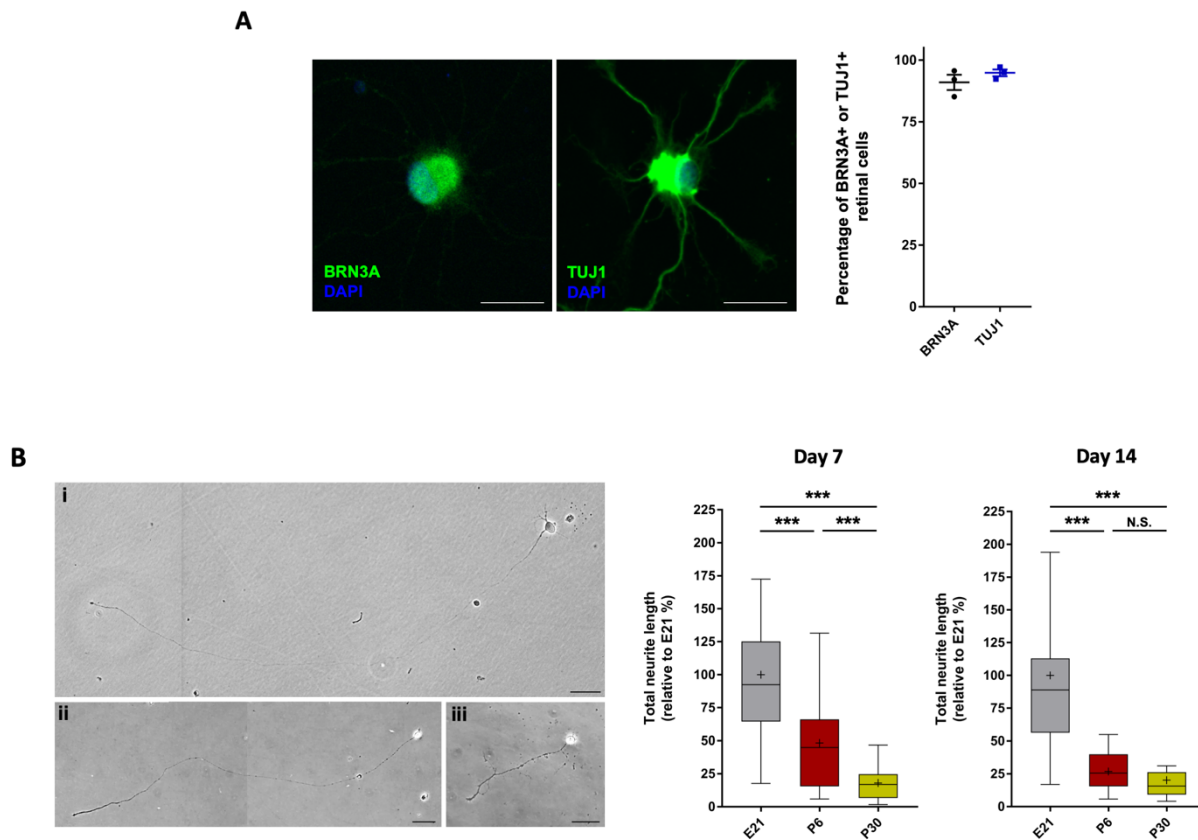
Supplemental Information

MicroRNA-19a-PTEN Axis Is Involved

in the Developmental Decline of Axon

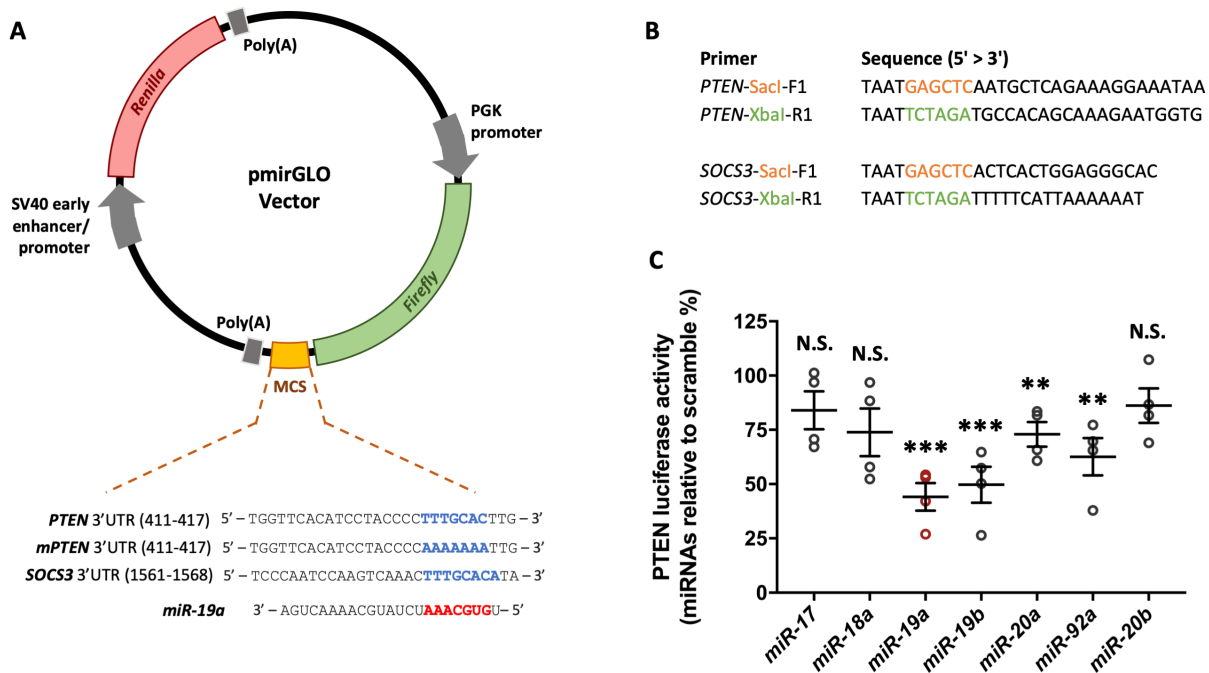**Regenerative Capacity in Retinal Ganglion Cells**

Heather K. Mak, Jasmine S.Y. Yung, Robert N. Weinreb, Shuk Han Ng, Xu Cao, Tracy Y.C. Ho, Tsz Kin Ng, Wai Kit Chu, Wing Ho Yung, Kwong Wai Choy, Chi Chiu Wang, Tin Lap Lee, and Christopher Kai-shun Leung

Figure S1. Developmental Decline of Axon Regenerative Capacity in Retinal Ganglion Cells.

(A) *(left)* Immunofluorescence images of BRN3A and TUJ1 staining of retinal ganglion cells (RGCs) isolated from Sprague Dawley (SD) rats using CD90.1 antibodies tagged with magnetic microbeads (Miltenyi Biotec). Scale: 25 μm. *(right)* Purity of RGC isolation was estimated from single-cell analysis of the proportion of BRN3A-positive or TUJ1-positive retinal cells (n=398 total retinal cells from 3 experimental replicates were counted). **(B)** *(left)* Bright field images of RGCs purified from (i) embryonic day 21 (E21), (ii) post-natal day 6 (P6), and (iii) post-natal day 30 (P30) SD rats. Scale bar: 50 μm. *(right)* The total neurite lengths were measured on day 7 and 14 *in vitro*. Single-cell analysis showed that P6 and P30 RGC neurite lengths were significantly shorter than those of E21 RGCs (Day 7: E21 vs. P6, p<0.0001; E21 vs. P30, p<0.0001; P6 vs. P30, p<0.0001; Day 14: E21 vs. P6, p<0.0001; E21 vs. P30, p<0.0001; P6 vs. P30, p=0.129; n=63 E21 RGCs, n=72 P6 RGCs, and n=84 P30 RGCs; n=2 experimental replicates). Unpaired two-tailed Student's t-test was used for all comparisons; ***p<0.001; N.S.=not significant. All boxes show the 25th, 50th (median), and 75th percentiles; + represents the data mean; whiskers follow a Turkey boxplot distribution (without outliers) and represent the lower and upper ranges of the data within 1.5x the interquartile range (IQR). All values are in mean ± SEM.

A

pmirGLO Vector

Poly(A)

Renilla

SV40 early enhancer/promoter

Poly(A)

MCS

PGK promoter

Firefly

PTEN 3'UTR (411-417) 5' – TGGTTCACATCCTACCCC**TTTGCAC**TTG – 3'
mPTEN 3'UTR (411-417) 5' – TGGTTCACATCCTACCCC**AAAAAAA**TTG – 3'
SOCS3 3'UTR (1561-1568) 5' – TCCCAATCCAAGTCAAAC**TTTGCACA**TA – 3'

miR-19a 3' – AGUCAAAACGUAUCU**AAACGUG**U– 5'

B

Primer	Sequence (5' > 3')
PTEN-SacI-F1	TAAT**GAGCTC**AATGCTCAGAAAGGAAATAA
PTEN-XbaI-R1	TAAT**TCTAGA**TGCCACAGCAAAGAATGGTG
SOCS3-SacI-F1	TAAT**GAGCTC**ACTCACTGGAGGGCAC
SOCS3-XbaI-R1	TAAT**TCTAGA**TTTTTCATTAAAAAAT

C

Figure S2. Construct Designs of Dual Luciferase Plasmids to Examine the Binding of miR-19a onto *PTEN, mPTEN,* and *SOCS3* 3'UTR in Retinal Ganglion Cells.

(A) The construct design of pmirGLO dual luciferase plasmid. Perfect complementarity of the miR-19a seed sequence *(red boldface)* onto miR-19a binding sites *(blue)* on *PTEN* and *SOCS3* 3'UTR would suppress translation of the *Firefly* luciferase transcript, which decreases *Firefly* luciferase activity, reducing emitted bioluminescent signals upon luciferin oxygenation. *mPTEN* 3'UTR sequence mutated miR-19a binding sites. All *Firefly* luciferase signals were normalized to *Renilla* luciferase signals that are unaffected by miR-19a binding as an endogenous control. MCS, multiple cloning site. **(B)** The primer sequences for cloning of *PTEN* and *SOCS3* 3'UTR into dual luciferase plasmids. **(C)** Dual luciferase assays of *PTEN* 3'UTR after transfection with miR-17, miR-18a, miR-19a, miR-19b, miR-20a, miR-92a, or miR-20b mimic oligos, compared with scramble oligos in P6 RGCs. There was a suppression of the PTEN luciferase by miR-19a, miR-19b, miR-20a, and miR-92a, respectively (miR-19a, $p=0.0001$; miR-19b, $p=0.001$; miR-20a, $p=0.003$; miR-92a, $p=0.005$; n=4 experimental replicates per group). miR-17 miR-18a, and miR-20b did not significantly suppress PTEN luciferase activity ($p \geq 0.055$). All *Firefly* luciferase was normalized to *Renilla* activity. All values are in mean ± SEM. Unpaired two-tailed Student's t-test was used for all comparisons; **$p<0.01$, ***$p<0.001$, N.S.=not significant.

A

| ITR | | U6 | miR-19a | CAG | eGFP | | ITR |

| ITR | | U6 | miR-19a TuD | CMV | eGFP | | ITR |

B

GATCCGACGGCGCTAGGATCATCAAC<mark>CAGTTTT*ccca*ATAGA<u>TTTGCACA</u></mark>CA
AGTATTCTGGTCACAGAATACAAC<mark>CAGTTTT*ccca*ATAGA<u>TTTGCACA</u></mark>CAAG
ATGATCCTAGCGCCGTCTTTTTTGAATTC

C

Fold-change of miR-19 expression (relative to AAV-eGFP)

● AAV-miR-19a-eGFP
□ AAV-miR-19aTuD-eGFP
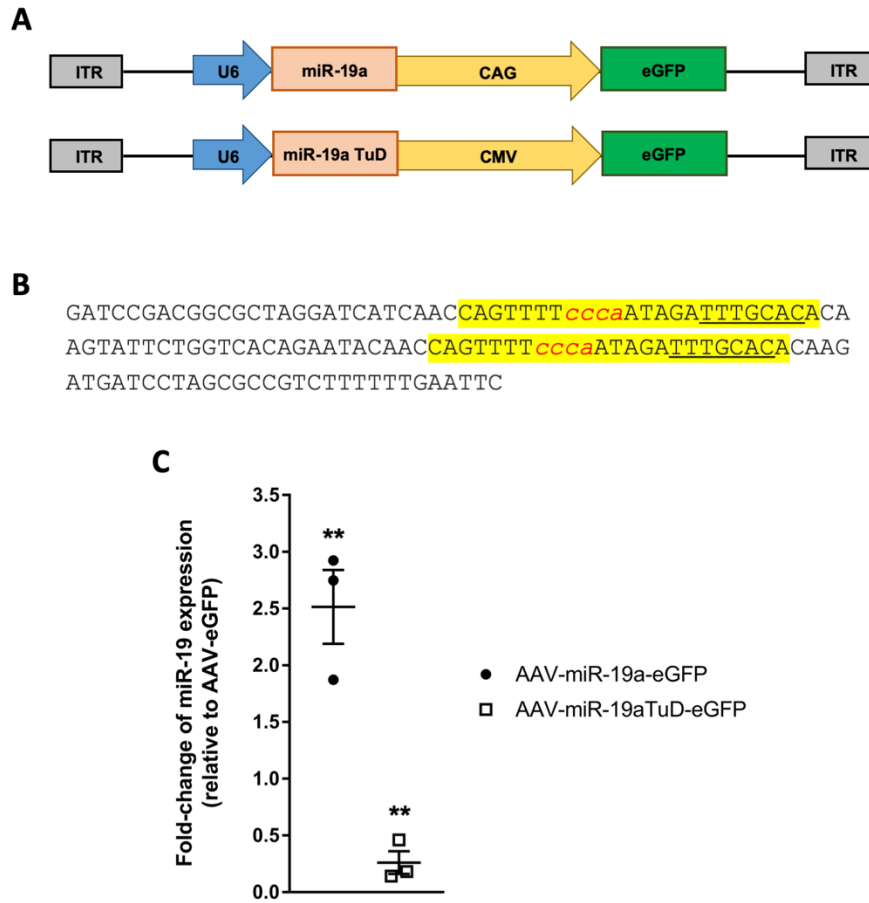
Figure S3. Construct Designs of Adeno-associated Virus (AAV) Plasmids for Delivery of miR-19a and miR-19a Tough Decoy (TuD) to Retinal Ganglion Cells.

(A) Schematic representation of the miR-19a- and miR-19aTuD-expressing AAV vectors. CAG, hybrid construct consisting the cytomegalovirus (CMV) enhancer fused to the chicken β-actin promoter, CMV, cytomegalovirus promoter, eGFP, enhanced green fluorescent protein, ITR, inverted terminal repeats, U6, U6 promoter. **(B)** Sequence of the miR-19a TuD construct. The miR-19a binding site is highlighted in yellow with miRNA seed sequence underlined. An RNA bulge for imperfect miRNA complementarity to enhance miRNA binding efficiency was induced using *ccca* inserts *(red italicized text)*. **(C)** miR-19a levels increased by 2.5±0.3-fold in RGCs transduced with AAV-miR-19a-eGFP, and decreased by 74±9.9% in RGCs transduced with AAV-miR-19aTuD-eGFP using TaqMan qRT-PCR (AAV-miR-19a-eGFP, p=0.010; AAV-miR-19aTuD-eGFP, p=0.002; n=3 experimental replicates per group). Expression values were normalized to AAV-eGFP-transduced P6 RGCs. All values are in mean ± SEM. Unpaired two-tailed Student's t-test was used for all comparisons; **p<0.01.
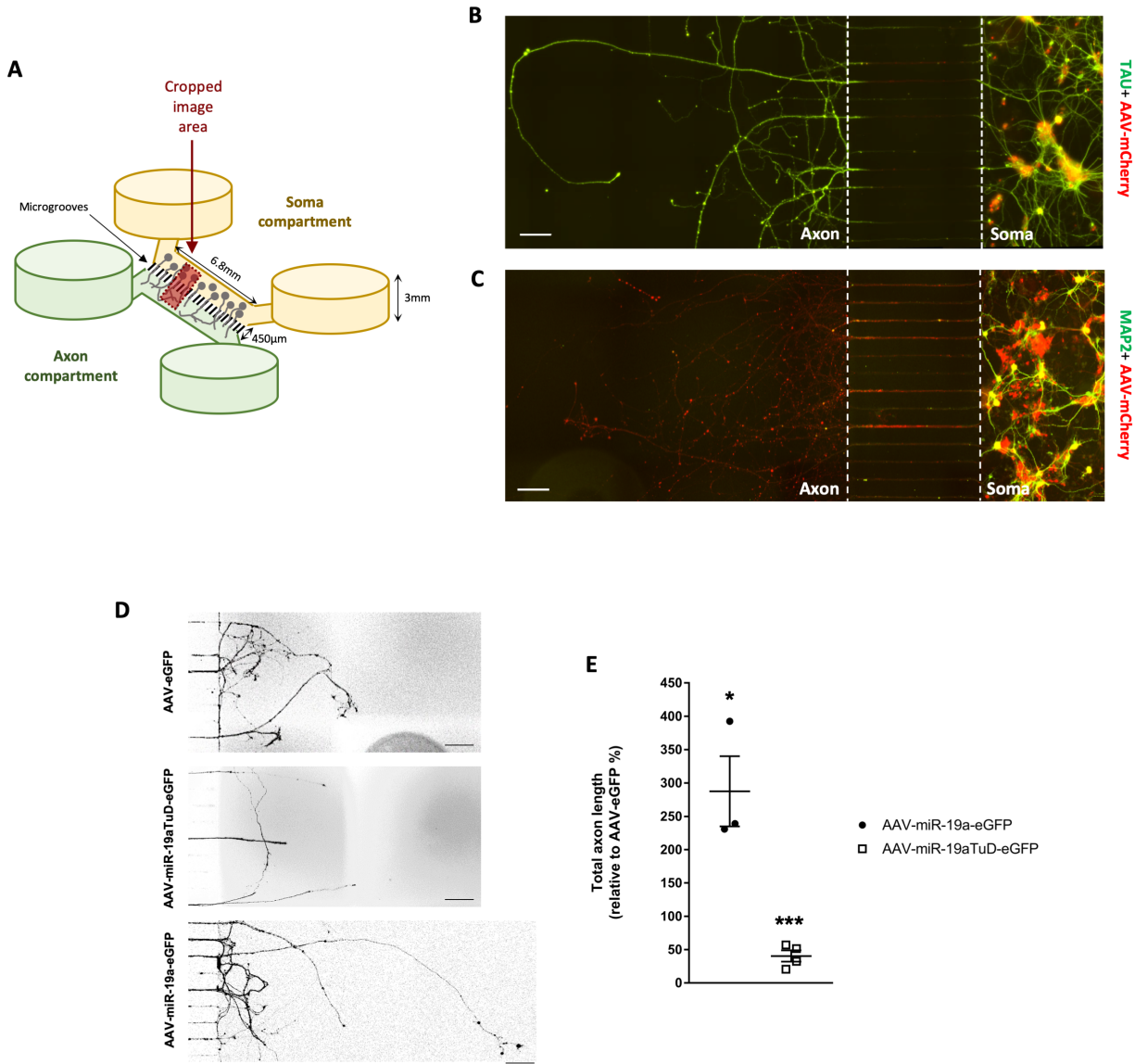
Figure S4. Immunofluorescence Staining of TAU and MAP2 in Retinal Ganglion Cells Cultured in Microfluidic Chambers and the Impact of Overexpression and Inhibition of miR-19a on Axon Extension.

(A) A figure illustration of the design and features of the microfluidic chamber. Cropped image areas of axon-specific TAU **(B)** and dendrite-specific MAP2 **(C)** immunofluorescence staining in P6 RGCs using a microfluidic chamber with indented microgrooves separating the axon from the soma. TAU is detected in both the soma and axon compartments *(left)*, whereas MAP2 remains only in the soma compartment *(right)*, confirming that only axons extend into the axon compartment of microfluidic chambers. AAV-mCherry was used to visualize the RGCs. Scale bar: 100 μm. **(D)** Fluorescence microscopy images of AAV-miR-19aTuD-eGFP- and AAV-miR-19a-eGFP-transduced P6 RGCs in cropped image areas of microfluidic chambers at day-in-vitro 14. Scale bar: 100 μm. **(E)** Comparisons of total axon length between AAV-miR-19aTuD-eGFP- (n=4 experimental replicates) or AAV-miR-19a-eGFP-transduced (n=3 experimental replicates) RGCs and AAV-eGFP-transduced RGCs (n=7 experimental replicates) on day 14 *in vitro*. Compared with AAV-eGFP-transduced P6 RGCs, axon lengths were significantly shorter in AAV-miR-19aTuD-eGFP-tranduced P6 RGCs and significantly longer in AAV-miR-19a-eGFP-transduced P6 RGCs (AAV-miR-19a-eGFP, p=0.034; AAV-miR-19aTuD-eGFP, p=0.0004). All values are in mean ± SEM. Unpaired two-tailed Student's t-test was used for all comparisons; *p<0.05; ***p<0.001.
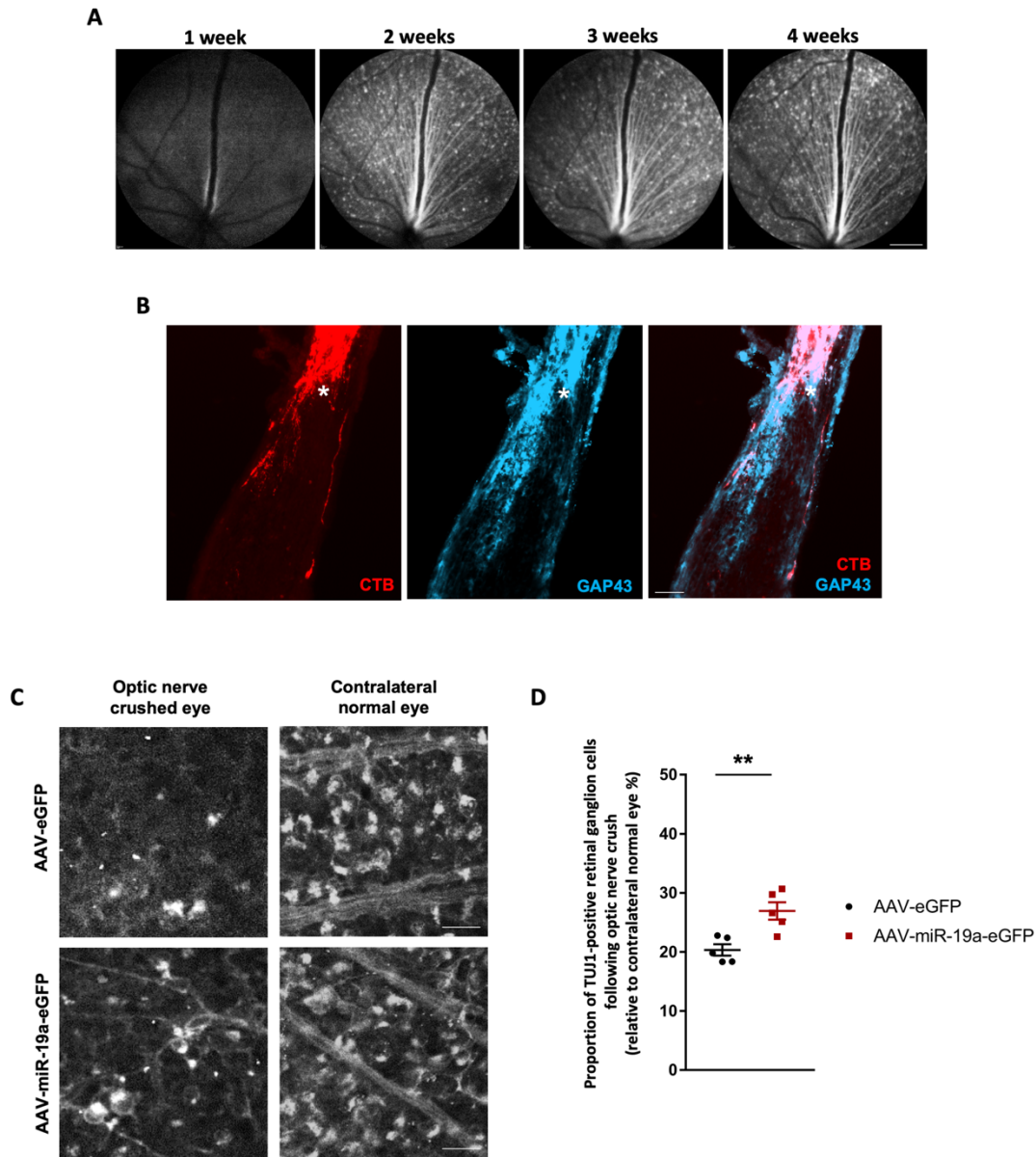
Figure S5. Time-lapse *In Vivo* Retinal Imaging After Intravitreal Injection of AAV-miR-19a-EGFP, Immunofluorescent Staining of GAP43 in the Optic Nerve, and Retinal Ganglion Cell Survival After Optic Nerve Crush.

(A) Confocal scanning laser ophthalmoscopy images of the retina of a C57BL/6J mouse at 1 week, 2 weeks, 3 weeks, and 4 weeks after intravitreal injection of AAV-miR-19a-eGFP. AAV transduction peaked at 2-3 weeks after the intravitreal injection. Scale bar: 200 μm. **(B)** Images of GAP43 *(blue)* immunofluorescence staining and CTB *(red)* in the optic nerve from an eye intravitreally injected with AAV-miR-19a-eGFP at 4 weeks following optic nerve crush. White asterisk indicates optic nerve crush site. Scale bar: 50 μm. **(C)** Images of immunofluorescence staining of TUJ1 in retinal whole-mounts after transduction with AAV-eGFP *(top)* or AAV-miR-19a-eGFP *(bottom)* at 4 weeks following optic nerve crush. Scale bar: 25 μm. **(D)** Proportion of TUJ1-positive retinal ganglion cells following optic nerve crush relative to contralateral normal eye (p=0.006; n=5 mice for each group). All values are in mean ± SEM. Unpaired two-tailed Student's t-test was used for all comparisons; **p<0.01.

Table S1. Microarray Analysis of Differentially Expressed MicroRNA in Retinal Ganglion Cells Purified from Embryonic Day 21 (E21) and Post-natal Day 30 (P30) Sprague Dawley Rats. Only microRNAs with ≥4-fold difference in the expression levels between E21 and P30 RGCs with Benjamini-Hochberg corrected p<0.05 are listed.

	E21 vs. P30		
miRNA	Regulation	Fold Change	p
rno-miR-17-5p	down	3742.68	1.67E-04
rno-miR-20b-5p	down	3549.30	1.67E-04
rno-miR-19a	down	2550.93	1.67E-04
rno-miR-18a	down	1771.39	1.67E-04
rno-miR-206	up	1522.66	7.09E-04
rno-miR-20a	down	1288.00	2.47E-02
rno-miR-216a	down	1222.42	2.57E-04
rno-miR-217	down	948.58	2.57E-04
rno-miR-216b-5p	down	739.71	2.57E-04
rno-miR-29c*	up	663.96	1.03E-03
rno-miR-301b	down	558.14	2.63E-04
rno-miR-330*	up	490.72	1.14E-03
rno-miR-370	down	452.93	3.69E-04
rno-miR-130b	down	422.48	4.46E-02
rno-miR-219-5p	down	360.41	4.27E-03
rno-miR-532-5p	down	339.67	2.63E-04
rno-miR-412*	up	255.90	1.73E-03
rno-miR-34b	down	239.96	2.54E-03
rno-miR-484	down	232.25	2.98E-04
rno-miR-34c	down	228.62	8.71E-04
rno-miR-322	down	222.98	5.74E-04
rno-miR-29a	up	214.24	2.98E-04
rno-miR-362*	down	209.71	6.69E-04
rno-miR-375	up	183.77	2.34E-03
rno-miR-31*	up	172.39	2.34E-03
rno-miR-363	down	158.35	3.69E-04
rno-miR-33	down	154.96	5.90E-03
rno-miR-488	down	150.82	1.03E-03
rno-miR-532-3p	down	146.02	7.19E-04
rno-miR-3559-5p	down	124.47	1.03E-03
rno-miR-134	down	114.61	9.26E-03
rno-miR-298	down	89.88	2.49E-03
rno-miR-3593-3p	down	86.47	3.17E-02
rno-miR-181c*	down	85.74	6.30E-04
rno-miR-374	down	84.62	6.69E-04
rno-miR-350	down	81.70	5.74E-04

rno-miR-129-2*	up	78.97	5.74E-04
rno-miR-325-5p	down	77.82	1.03E-03
rno-miR-423*	down	73.93	4.48E-03
rno-miR-129-1*	up	65.63	1.14E-03
rno-miR-211	up	60.19	1.84E-02
rno-miR-130b*	down	53.86	1.18E-03
rno-miR-20a*	down	49.36	8.71E-04
rno-miR-129	up	30.57	2.49E-03
rno-miR-99b*	down	29.13	2.49E-03
rno-miR-19b	down	27.80	1.59E-03
rno-miR-31	up	17.40	4.67E-03
rno-miR-92a	down	15.90	3.16E-03
rno-miR-106b	down	14.27	3.40E-03
rno-let-7b	up	14.14	2.83E-03
rno-miR-485	up	12.32	4.67E-03
rno-miR-29c	up	11.46	3.91E-03
rno-miR-93	down	10.78	5.09E-03
rno-miR-132	up	10.32	8.98E-03
rno-let-7c	up	9.26	5.09E-03
rno-miR-383	up	9.26	9.35E-03
rno-let-7d	up	7.32	8.21E-03
rno-miR-130a	down	7.25	1.13E-02
rno-miR-664	up	7.03	2.79E-02
rno-miR-301a	down	6.55	3.07E-02
rno-miR-127	up	6.47	1.26E-02
rno-miR-183	up	6.38	1.84E-02
rno-miR-328a	up	6.26	1.60E-02
rno-miR-128	up	6.25	1.39E-02
rno-miR-7a	up	5.94	3.49E-02
rno-miR-431	down	5.60	1.71E-02
rno-miR-539	up	5.47	4.92E-02
rno-miR-15b	down	5.28	2.02E-02
rno-miR-146b	up	5.17	3.63E-02
rno-miR-25	down	4.86	1.77E-02
rno-miR-376b-5p	up	4.59	2.85E-02
rno-miR-329	up	4.58	3.63E-02
rno-let-7f	up	4.56	2.85E-02
rno-miR-23b	up	4.53	2.53E-02
rno-miR-341	down	4.46	2.79E-02
rno-let-7a	up	4.19	2.85E-02

Table S3. List of Primary and Secondary Antibodies for Immunocytochemistry (ICC) and Western Blot (WB).

Antibody	Source (Catalog Number)	Working Concentration
Primary antibodies		
Mouse monoclonal anti-beta-Actin clone AC-15	Sigma (A3854)	WB 1:10,000
Rabbit monoclonal anti-BRN3A	Abcam (ab81213)	ICC 1:50
Rabbit polyclonal anti-GAP43	Abcam (ab12274)	ICC 1:200
Mouse monoclonal anti-GAPDH	Thermo Fisher (AM4300)	WB 1:10,000
Mouse monoclonal anti-MAP2	Upstate (05-346)	ICC 1:200
Rabbit monoclonal anti-PTEN	Cell Signaling (9559)	ICC 1:100, WB 1:500
Mouse monoclonal anti-SOCS3	Abcam (ab14939)	WB 1:500
Rabbit monoclonal anti-TAU	Abcam (ab32057)	ICC 1:200
Mouse monoclonal anti-TUJ1	Millipore (MAB5564)	ICC 1:200
Rabbit polyclonal anti-TUJ1	Covance (PRB-425P)	ICC 1:500
Secondary antibodies		
Goat anti-rabbit Alexa Fluor® 350	Invitrogen (A-21068)	ICC 1:1000
Goat anti-mouse Alexa Fluor® 488	Invitrogen (A-11001)	ICC 1:1000
Goat anti-rabbit Alexa Fluor® 488	Invitrogen (A-11008)	ICC 1:1000
Goat anti-mouse Rhodamine Red	Invitrogen (R-6393)	ICC 1:1000
Goat anti-rabbit Rhodamine Red	Invitrogen (R-6394)	ICC 1:1000

Table S2. A Cluster of 314 Downstream Targets of the miR-17-92 Family with Significant Association with Neuron Projection Development Using the PANTHER Classification System.

Video S1. Axon Regeneration of a Retinal Ganglion Cell Transduced with AAV-miR-19a-EGFP After Axotomy.

Video S2. Axon Regeneration of a Retinal Ganglion Cell Transduced with AAV-EGFP After Axotomy.

Data S1. Customized MATLAB program for single-cell analysis of RGC axon length and total neurite length.

Data S2. Customized MATLAB program for microfluidic chamber analysis of total RGC axon length.